

Correlating the structural transformation and properties of ZIF-67 during
pyrolysis, towards electrocatalytic oxygen evolution

*Sara Frank, Mads Folkjær, Mads L. N. Nielsen, Melissa J. Marks, Henrik S. Jeppesen,
Marcel Ceccato, Simon J. L. Billinge, Jacopo Catalano* and Nina Lock**

Electronic Supporting Information

Table of contents

1. Rietveld refinement of pristine ZIF-67
2. TGA – different heating ramps
3. *In situ* hard X-ray techniques
 - 3.1 X-ray absorption spectroscopy
 - 3.1.1 Linear combination analysis (LCA)
 - 3.1.1.1 Against Co and ZIF-67
 - 3.1.1.2 Against first and last frame
 - 3.1.1.3 Against Co, ZIF-67 and CoO
 - 3.1.2 EXAFS
 - 3.2 Total scattering
 - 3.2.1 NMF analysis
 - 3.2.2 Fingerprinting analysis
4. *Ex situ* structural characterization
 - 4.1 Thermal analysis
 - 4.2 Transmission electron microscopy (TEM)
 - 4.3 Gas adsorption measurements
 - 4.4 XAS
 - 4.4.1 LCA fits
 - 4.5 PDF
 - 4.5.1 The local structure
 - 4.5.2 PDF fits
 - 4.5.2.1 One phase refinements
 - 4.5.2.2 Two phase refinements
 - 4.5.2.3 Sliding boxcar refinements
 - 4.5.2.4 Sliding r_{\max} refinements
5. Electrocatalytic OER
 - 5.1 Linear sweep voltammetry (LSV)
 - 5.2 Electrochemically active surface area (ECSA)
 - 5.3 Multistep electrolysis
 - 5.4 Chronopotentiometry
 - 5.5 Normalization to m_{Co} and ECSA
 - 5.6 Comparison with recent OER catalysts

1. Rietveld refinement of pristine ZIF-67

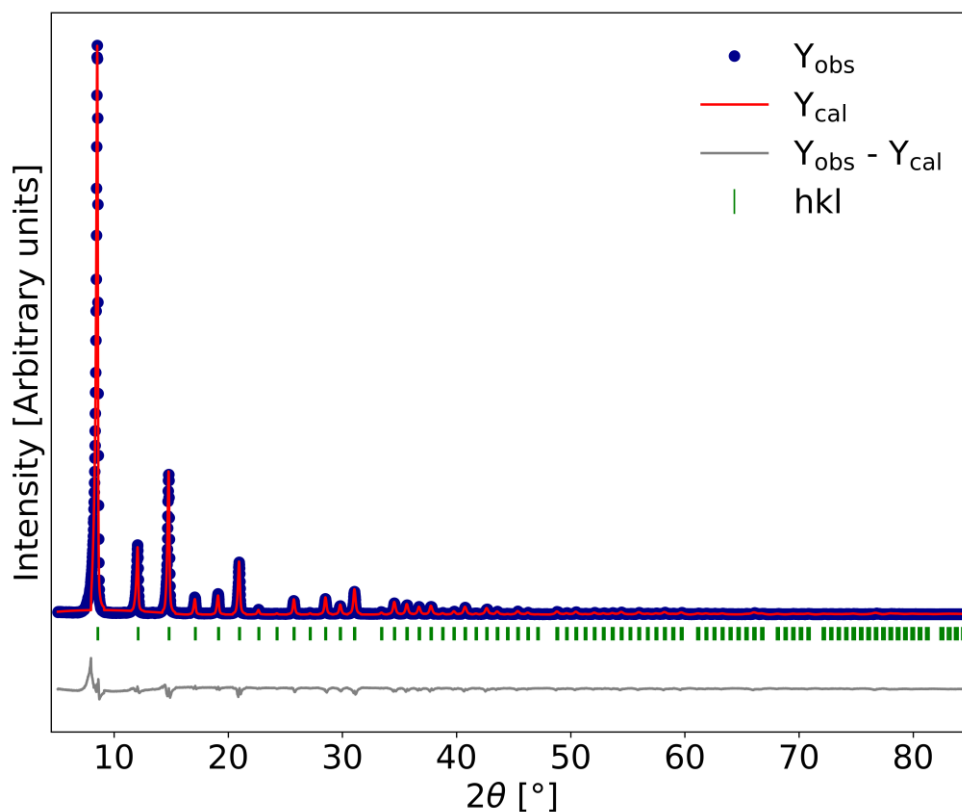


Fig. S1: Rietveld refinement of pristine ZIF-67 recorded using Co K α radiation.

Empirical formula	CoN₄C₈H₁₀
Crystal system	Cubic
Space group	<i>I</i> -43 <i>m</i>
$a = b = c$ [Å]	17.0817(3)
$\alpha = \beta = \gamma$ [°]	90
V [Å ³]	4984.2(2)
Bragg R-factor [%]	10.4
Rf-factor [%]	20.1

Table S1: Refinement results.

A sixth-degree polynomial was used to describe the background. The peak shapes were modeled by using the Thompson-Cox-Hastings pseudo-Voigt function. Due to the data quality of the lab source diffractometer atomic positions and B -factors were not refined.

The refinement primarily serves as a phase identification and purity check of the synthesized ZIF-67 (CCDC 671074¹).

2. TGA

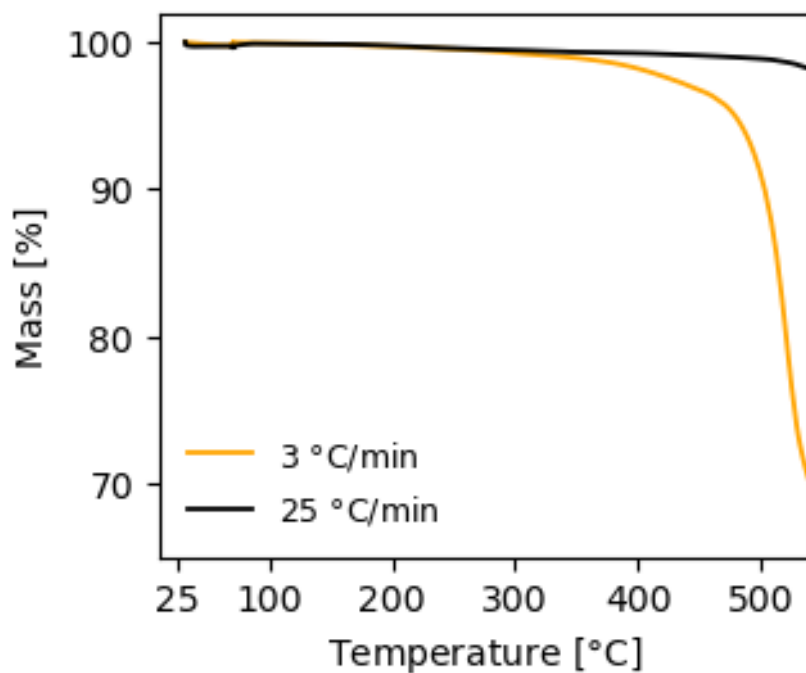


Fig. S2: Thermogravimetric analysis with different heating rates (3 °C min^{-1} and 25 °C min^{-1}) and a target temperature of 550 °C . With the slower heating rate of 3 °C min^{-1} , a mass loss of approx. 33% has occurred. With a rate of 25 °C min^{-1} a mass loss of only 2% is observed. The duration of a pyrolysis process with a heating rate of 3 °C min^{-1} takes approx. 3 hours, compared with a heating rate of 25 °C min^{-1} , which takes only approx. 22 min.

3. *In situ* X-ray-based structural characterization

3.1 X-ray Absorption spectroscopy

3.1.1 Linear combination analysis (LCA)

3.1.1.1 Co and ZIF-67 as references

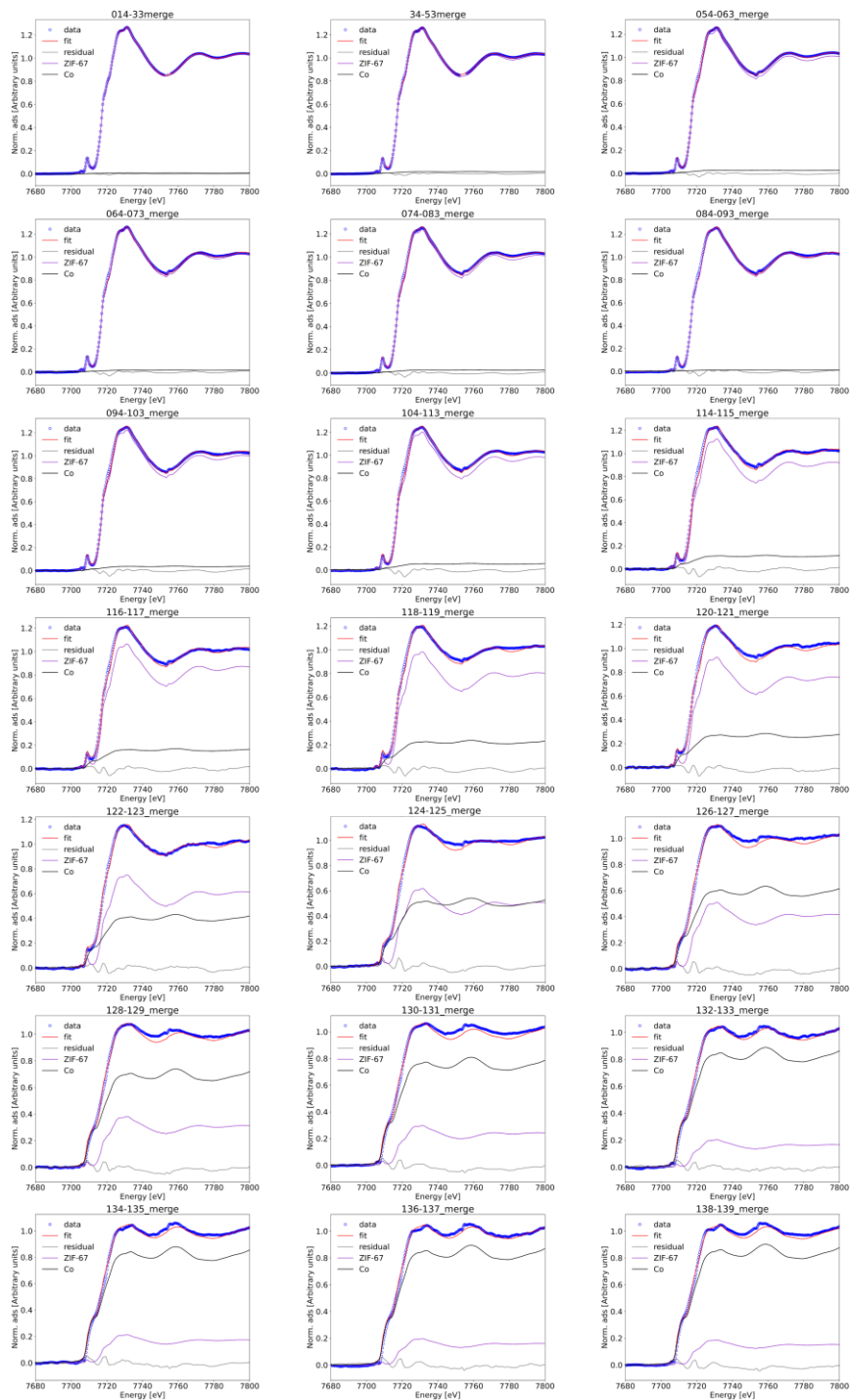


Fig. S3: LCA fits with ZIF-67 and metallic Co as reference spectra. E_0 is fixed and the sum of the weights is constrained to 1.

Frame number	Average $T / ^\circ\text{C}$	Weight ZIF-67	Weight Co	R -factor	Chi-square	Reduced Chi-square
014-033	96.3	0.992(1)	0.008(1)	0.0000334	0.00131	0.0000085
034-053	182.3	0.983(3)	0.017(3)	0.0001212	0.00470	0.0000303
054-063	246.5	0.973(4)	0.027(4)	0.0002554	0.00990	0.0000639
064-073	287	0.985(5)	0.015(5)	0.0003941	0.01538	0.0000992
074-083	327.5	0.976(5)	0.024(5)	0.0004060	0.01581	0.0001026
084-093	32.5	0.990(6)	0.010(6)	0.0006072	0.02403	0.0001560
094-103	411.5	0.964(7)	0.036(7)	0.0007536	0.02928	0.0001889
104-113	452	0.947(8)	0.053(8)	0.0011998	0.04655	0.0003023
114-115	479.5	0.888(11)	0.112(11)	0.0019426	0.07328	0.0004728
116-117	486	0.838(9)	0.162(9)	0.0015230	0.05627	0.0003654
118-119	495	0.775(9)	0.225(9)	0.0016346	0.05834	0.0003788
120-121	503	0.730(11)	0.270(11)	0.0023030	0.08222	0.0005305
122-123	510	0.592(9)	0.408(9)	0.0015364	0.05008	0.0003252
124-125	522.5	0.487(12)	0.513(12)	0.0036018	0.10200	0.0006624
126-127	527.5	0.401(13)	0.599(13)	0.0041929	0.11371	0.0007384
128-129	535	0.301(12)	0.699(12)	0.0037397	0.09883	0.0006376
130-131	545	0.234(12)	0.766(12)	0.0039708	0.10118	0.0006528
132-133	550	0.160(10)	0.840(10)	0.0026413	0.06182	0.0004014
134-135	550	0.167(10)	0.833(10)	0.0027326	0.06626	0.0004303
136-137	550	0.154(11)	0.846(11)	0.0031862	0.07486	0.0004861
138-139	550	0.147(10)	0.853(10)	0.0027056	0.06540	0.0004219

Table S2: Fitted phase content values.

3.1.1.2 The first and last frame as references

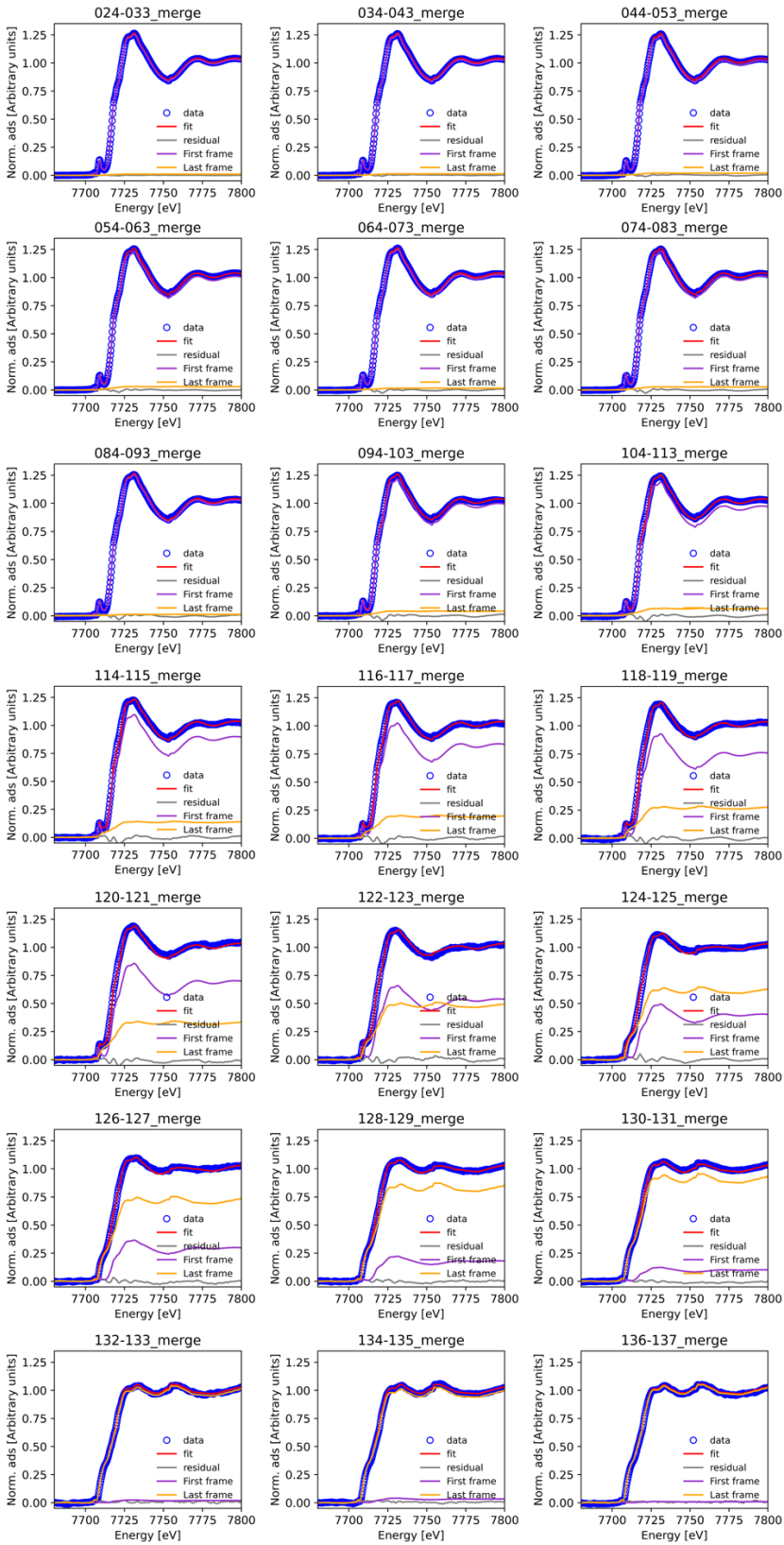


Fig. S4: LCA fits against first and last frame.

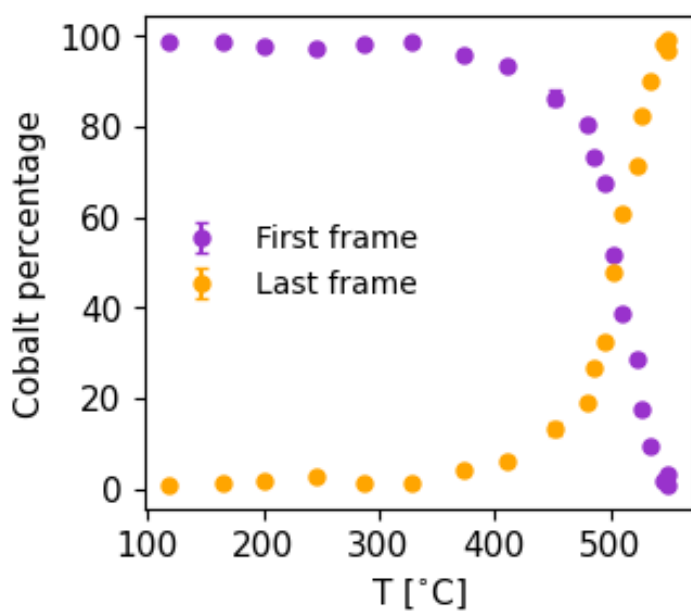


Fig. S5: LCA fits against the first and last frame as references indicating the evolution of the conversion process.

3.1.1.3 Co, ZIF-67, and CoO as references

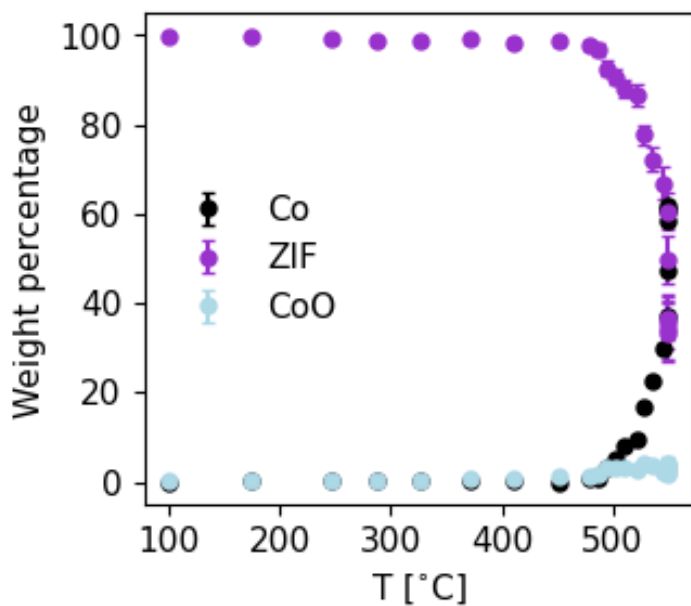


Fig. S6: LCA fits against the three references of metallic Co, pristine ZIF-67, and Co(II) oxide. Above 450 °C, as the weight percentage of Co starts to increase, a small fraction of the sample can be attributed to Co(II) oxide.

3.1.2 EXAFS

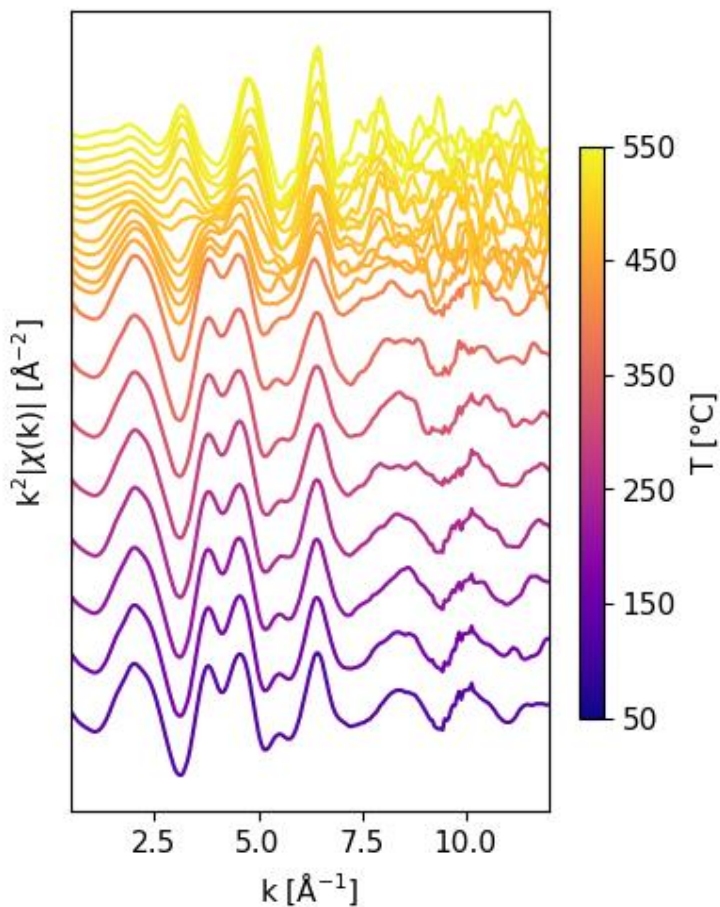


Fig. S7: EXAFS data in k -space. The data is k^2 -weighted. Glitches above 8\AA^{-1} have been removed. For the high temperature spectra, the signal above 7.5\AA is too noisy to distinguish features.

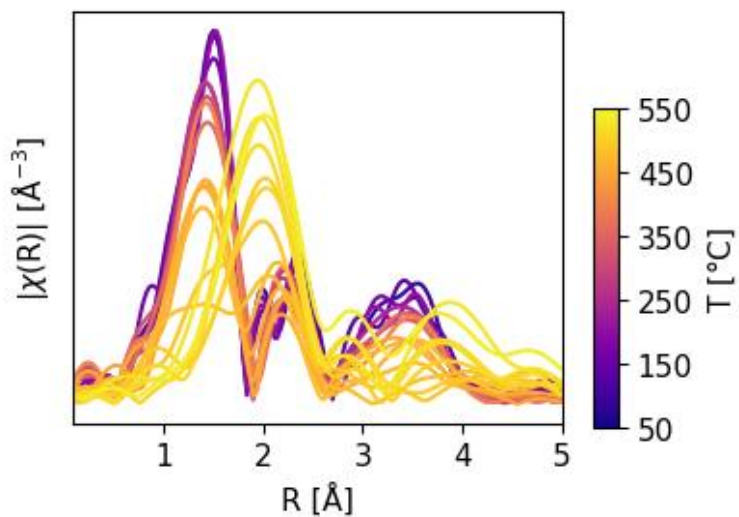


Fig. S8: Fourier transform of the EXAFS. Overlaid spectra are shown to highlight shifts in the nearest neighbor peak.

3.2 Total scattering

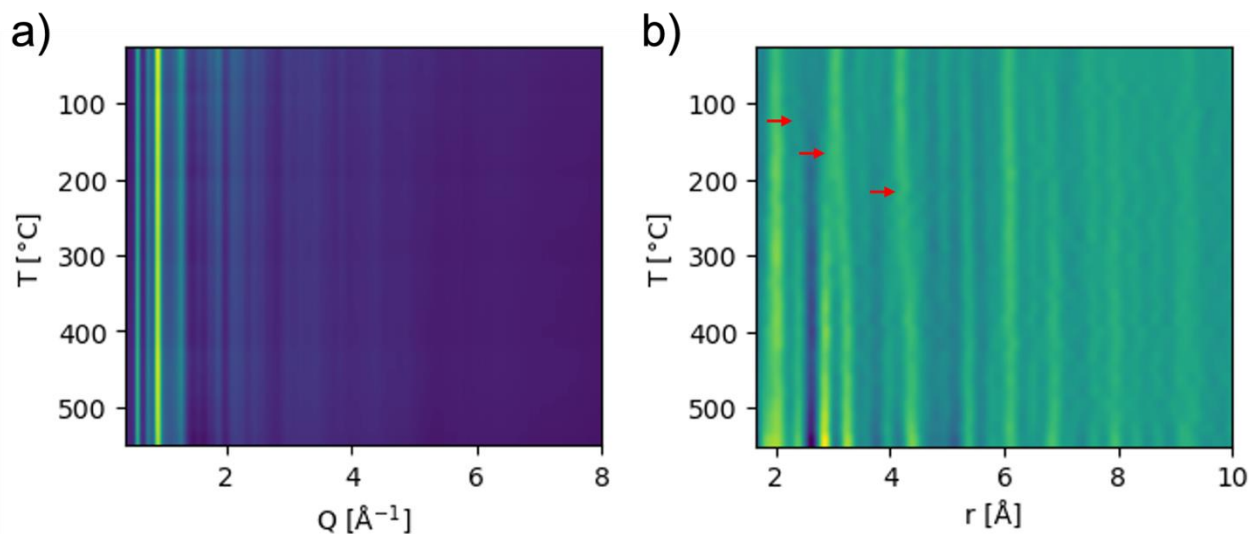


Fig. S9: a) Evolution of the intensity vs scattering vector Q with temperature. b) Evolution of the PDF as a function temperature. The red arrows indicate structural changes before the decomposition temperature between 100 °C and 300 °C.

3.2.1 NMF analysis

NMF analysis was performed with the *nmfMapping* application on the ‘PDF in the cloud’ platform.²

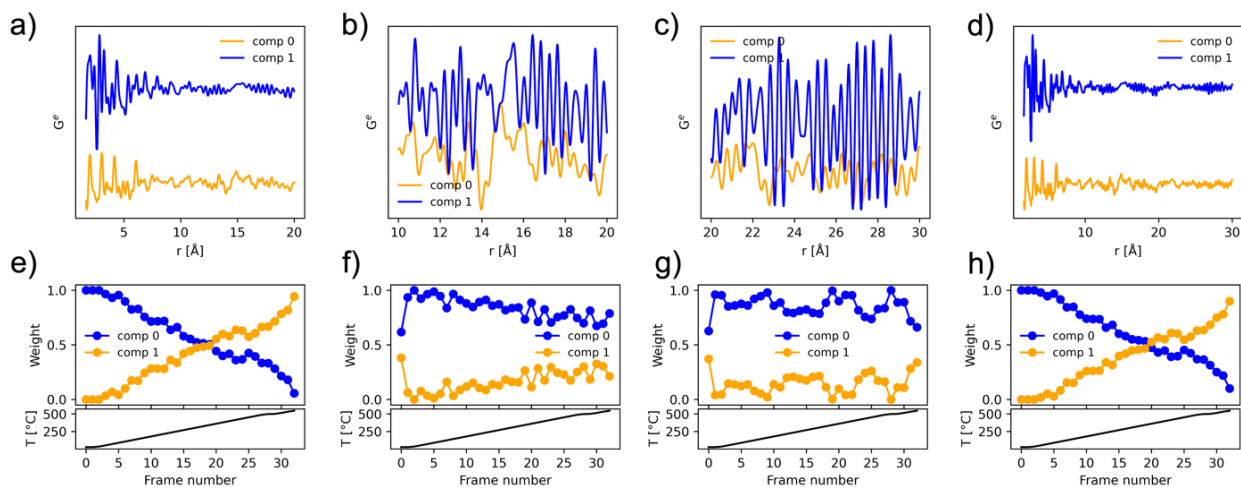


Fig. S10: a-d) NMF components. e-h) Evolution of components along with the temperature profile. In the r -range of a,e) 1.65-20 \AA , b,f) 10-20 \AA , c,g) 20-30 \AA , and d,h) 1.65-30 \AA . The analysis indicates that beyond 10 \AA there is little to few systematic changes, as well as indicating there is a higher noise level.

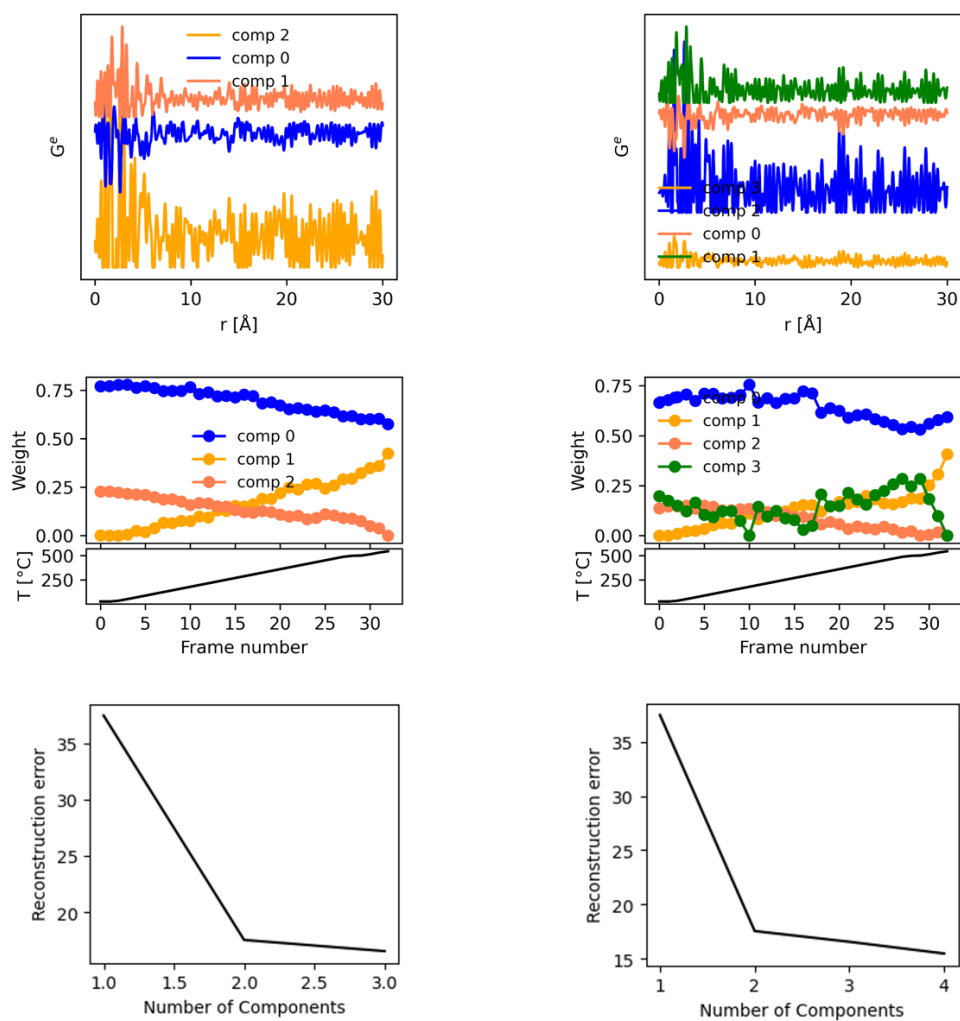


Fig. S11: NMF analysis with 3 and 4 components. The components become less similar to real PDFs. Very little structural information can be gathered, and only a minor improvement in the reconstruction error is observed. Thus, it is estimated that two components are sufficient to describe the changes observed during the *in situ* pyrolysis.

3.2.2 Fingerprint analysis

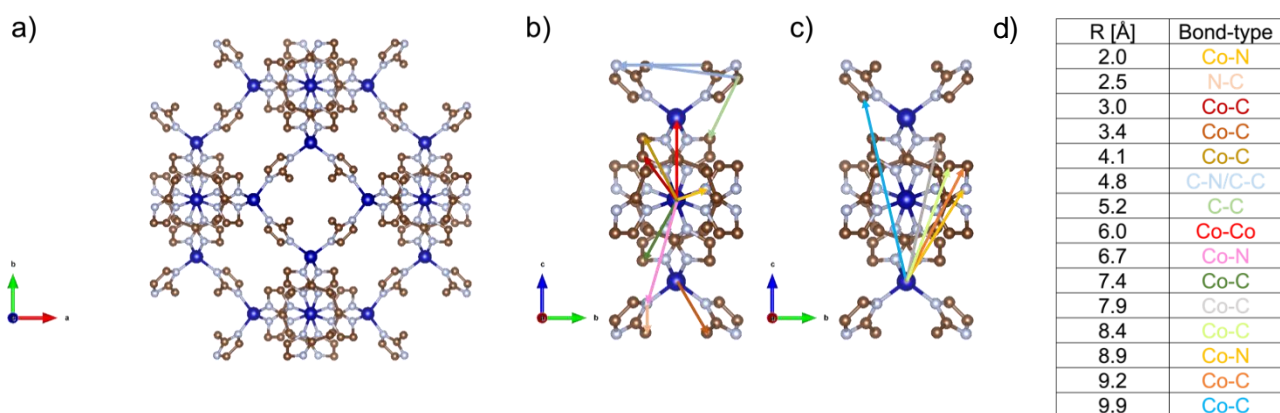


Fig. S12: a) Cubic ZIF-67 structure b,c) Cut-out of ZIF-67 structure with scattering paths shown as differently colored arrows. Figures made with VESTA.³ d) Distances of the different colored paths.

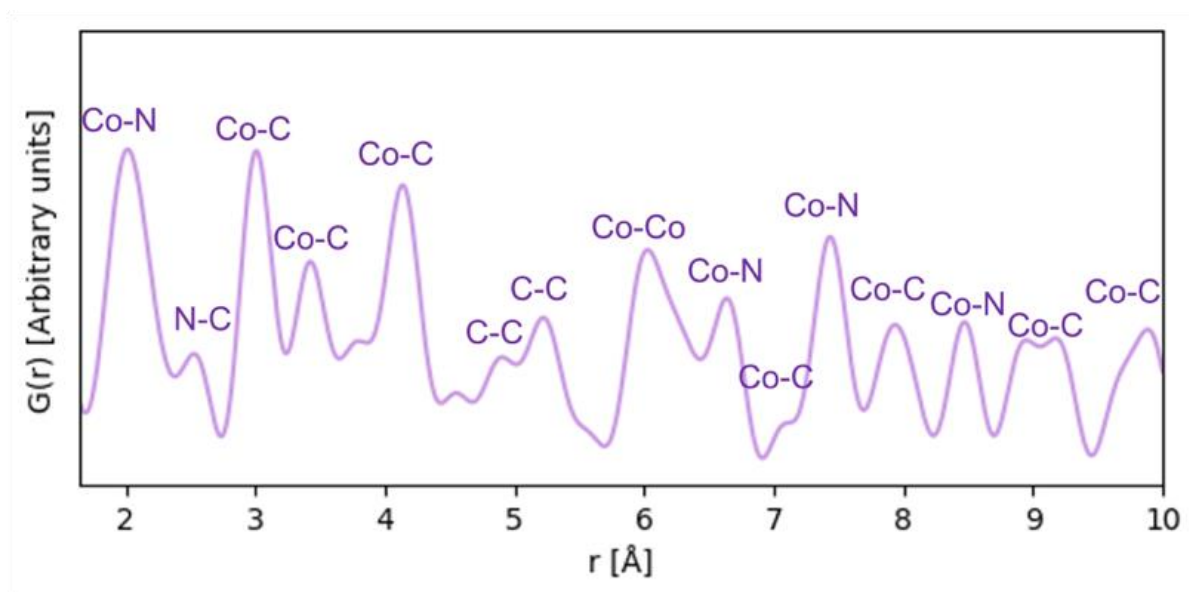


Fig. S13: Assignment of peaks in the calculated PDF of pristine ZIF-67. Calculated with PDFgui,⁴ based on the crystal structure from CCDC 671074.¹

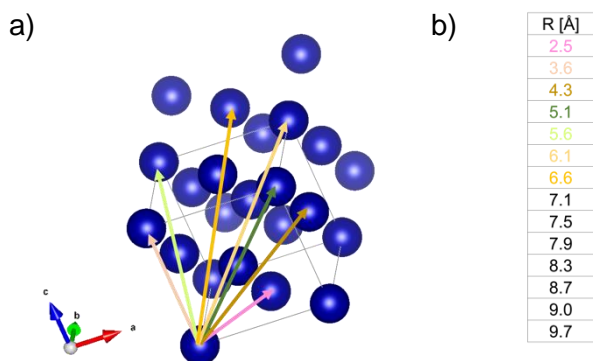


Fig. S14: a) Cubic Co fcc crystal structure. Different scattering paths are indicated with differently colored arrows. Figure made with VESTA.³ b) Distances of the different Co-Co paths.

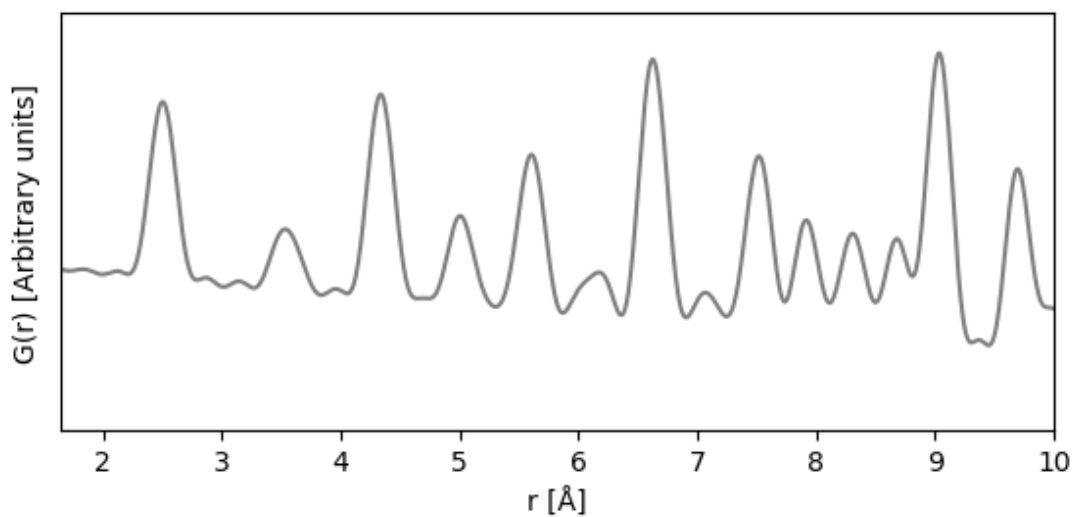


Fig. S15: The calculated PDF of Co fcc. Calculated with PDFgui,⁴ based on the crystal structure from ICSD 76632.⁵

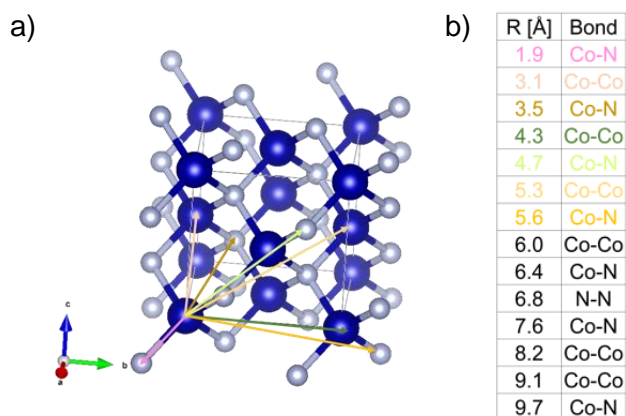


Fig. S16: a CoN crystal structure. Different scattering paths are indicated with differently colored arrows. Figure made with VESTA.³ b) Distances of the different scattering paths.

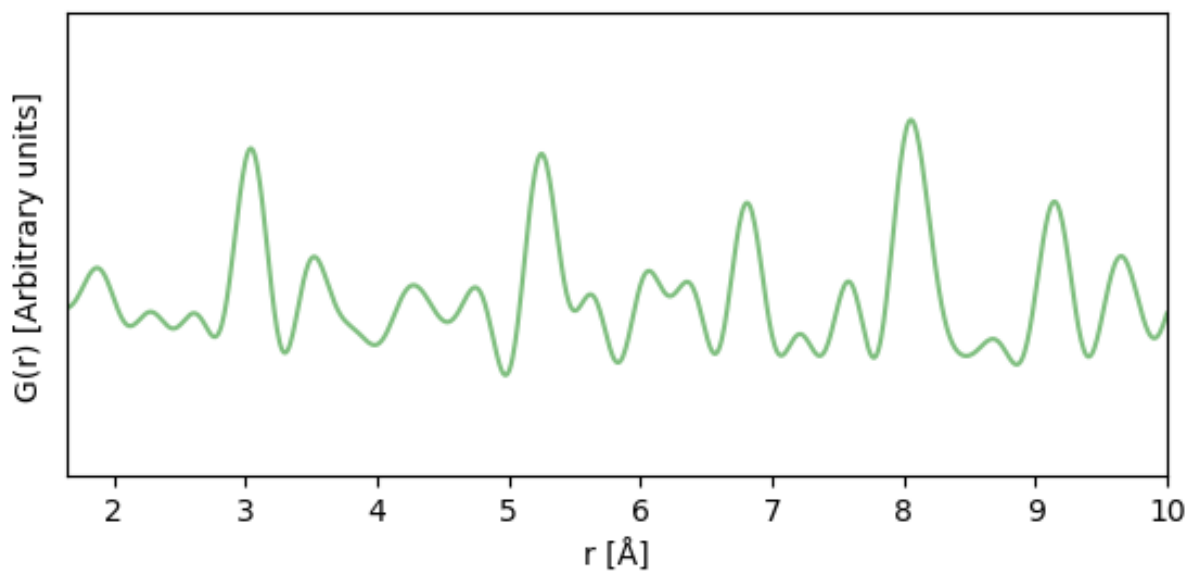


Fig. S17: The calculated PDF of CoN. Calculated with PDFgui,⁴ based on the crystal structure from ICSD 79936.⁶

4. *Ex situ* structural characterization

4.1 Thermogravimetric analysis

Thermogravimetric analysis (TGA) tests were conducted dynamically by continuously changing the temperature throughout the measurement (black curve Fig. S18a), but also by mimicking the *ex situ* pyrolysis durations, *i.e.* with an isothermal region at 550 °C for 12 hours (orange curve in Fig. S18a). TGA analysis was conducted on both ZIF-67 (Fig. S18a) and the reactants used for synthesizing ZIF-67 (Fig. S18c). For all the TGA experiments, an initial isothermal stage at 70 °C (2 hours) was carried out to remove any possible residual solvent or moisture.

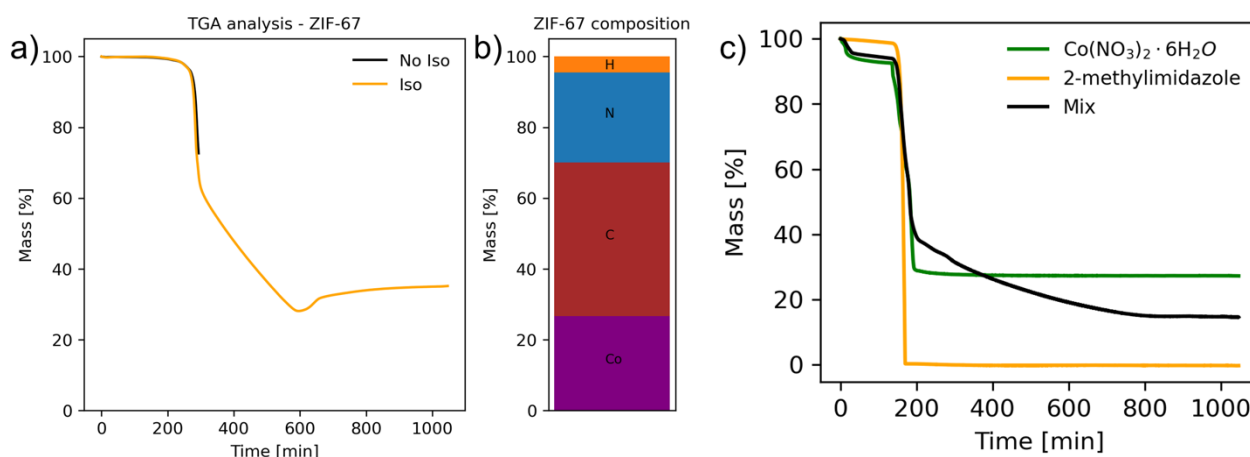


Fig. S18: a) TGA analysis, with the residual mass versus temperature measured with a heating ramp of 3 °C min⁻¹ from room temperature to a target temperature of 550 °C with no isothermal stage (black line) and with an isothermal stage at 550 °C for 12 h before a last heating step to 650 °C (orange line). b) Bar plot representing the ZIF-67 composition in wt%, ranked according to the element volatility with the lowest volatility at the bottom. c) TGA analysis conducted on the reactants for the ZIF-67 synthesis. All TGA measurements were performed under inert conditions with a flow of nitrogen of 20 mL min⁻¹. TGA measurements with an isothermal stage were carried out with the following settings: 30-70 °C (3 °C min⁻¹), 70 °C (time: 2 hours), 70-550 °C (3 °C min⁻¹), 550 °C (time: 12 hours) and 550-650 °C (3 °C min⁻¹). The non-isothermal measurement (the black line in panel a) was performed with the following settings: 30-70 °C (3 °C min⁻¹), 70 °C (time: 2 hours), 70-550 °C (3 °C min⁻¹).

During the initial heating to 550 °C, the ZIF-67 samples (both with and without the isotherm) experience a reduction of about 30% of their initial mass. After this initial mass loss, a continuous loss of mass over the next 12 hours can be observed in the isothermal segment. This indicates that long pyrolysis times might be needed to achieve a stable material since the material continuously undergo transformations.

A mass gain was observed in the TGA data after 600 min which is unusual for pyrolysis processes, given the inert atmosphere. As this mass gain proceeds over a significant amount of time, it is not a momentary glitch in the data. However, we tend to interpret this mass gain as an artefact in the measurement itself. Indeed, this phenomenon only appeared in the measurements of ZIF-67

conducted at the lowest scan rate ($3\text{ }^{\circ}\text{C min}^{-1}$ independent upon the target temperature, see Fig. S19b) while it is not present for the highest scan rate performed in this work ($25\text{ }^{\circ}\text{C min}^{-1}$). Also, no condensed organics compounds were found in the FT-IR analysis after the tests (see discussion of Fig. S21). In any case, the mass gain of the sample only constitutes around 4% of the original mass of the sample (13% considering the final residual mass), and does not change the conclusions of the TGA interpretation.

In Fig. S18, the TGA of the reactants used in the synthesis of ZIF-67 discloses that the unreacted reagents decompose at around $180\text{ }^{\circ}\text{C}$ and the residual mass must be ascribed to Co.

4.1.1: Comparison between the two different heating rates

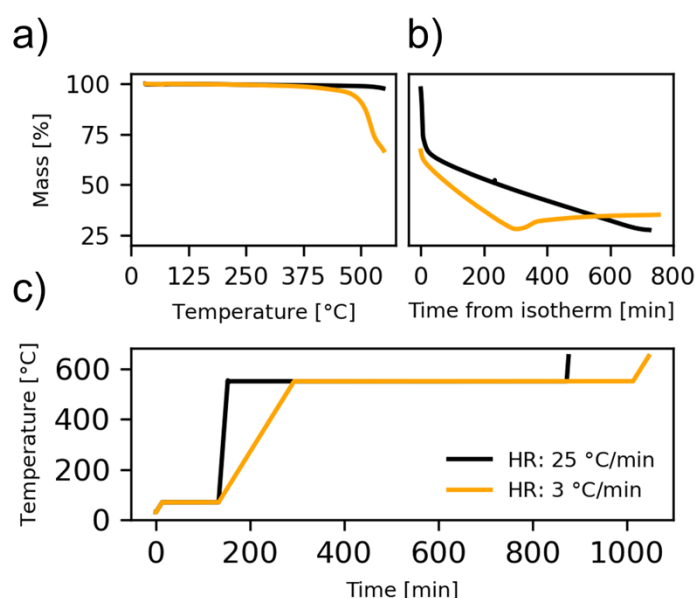


Fig. S19: a) Results from TGA measurements with isothermal stages compared for the two different heating rates of $3\text{ }^{\circ}\text{C min}^{-1}$ and $25\text{ }^{\circ}\text{C min}^{-1}$ (orange and black lines, respectively). a) The residual mass over the temperature range $30\text{--}550\text{ }^{\circ}\text{C}$, *i.e.* before the isothermal segment. b) The residual mass versus time during the isothermal stage. c) The temperature profile used in the experiments.

TGA measurements performed at different scan rates (Fig. S19) show that while a significant delay in the mass loss is observed at the high temperature rate, the end points of the two measurements are quite similar. This indicates that pyrolysis conducted at high temperature rates results in samples out of equilibrium, and again that longer pyrolysis time is needed to achieve equilibrium compounds.

As noted above, no mass gain is evident with the faster heating rate ($25\text{ }^{\circ}\text{C min}^{-1}$) experiment.

4. 1. 2: Isothermal segment at two different target temperatures and IR

TGA experiments were conducted at two different target temperatures for the isotherm region of 550 °C and 800 °C with the same scan rate of 3 °C min⁻¹ (Fig. S20).

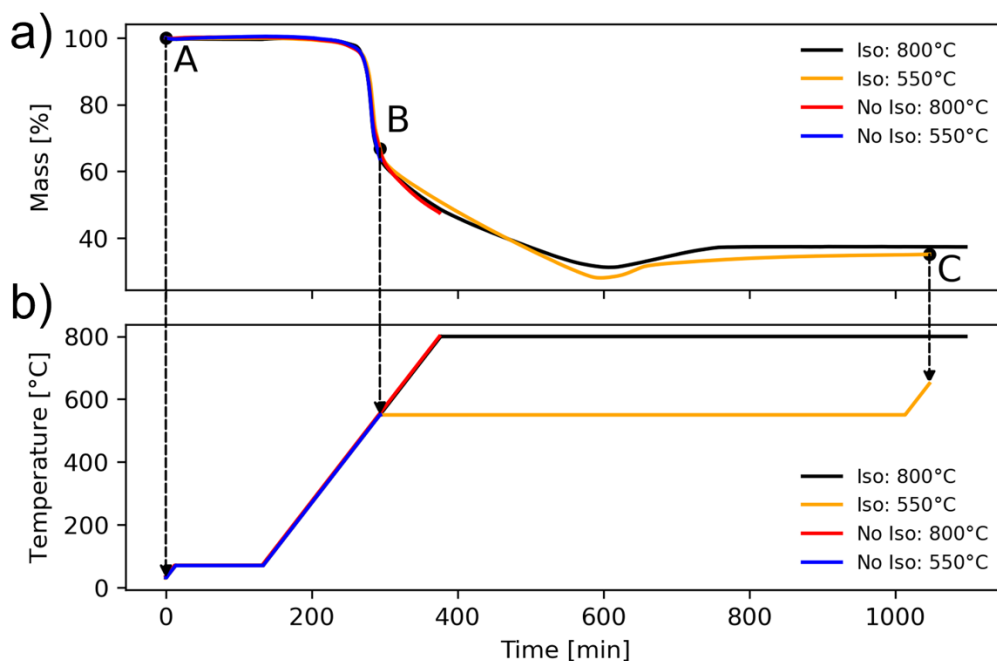


Fig. S20: a) TGA analysis with the residual mass versus time measured with a heating ramp of 3 °C min⁻¹. Blue line: from room temperature to 550 °C; orange line: from room temperature to 550 °C followed by an isothermal stage of 12 h and a final heating step to 650 °C. Red line: from room temperature to 800 °C. Black line: from room temperature to 800 °C followed by an isothermal stage of 12 h. b) The temperature profiles of the TGA measurements. Datapoints annotated with arrows indicate at which point samples were extracted for FT-IR analysis (see Fig. S21 for the FT-IR results).

Interestingly, experiments conducted at the different target temperatures but at the same heating rate, show an almost identical time evolution of the mass loss (Fig. S20b). This implies that once an onset temperature is achieved, the mass loss is independent on the temperature, or in other words, has a very low or almost zero activation energy. However, it is worth noting that these results strictly apply to the mass loss and no information on the catalyst structure can be drawn from these data. In any case, from the TGA alone it would appear that sample pyrolyzed at 650 °C without any isothermal stage should have intermediate characteristics between the ones pyrolyzed at 550 °C with 0 and 4 h isothermal stage.

Elucidating the chemical structure at the different stages of pyrolysis is attempted through FT-IR analysis on samples extracted at different pyrolysis times. Fig. S20 annotates when samples were extracted to perform FT-IR analysis; those results are reported in Fig. S21.

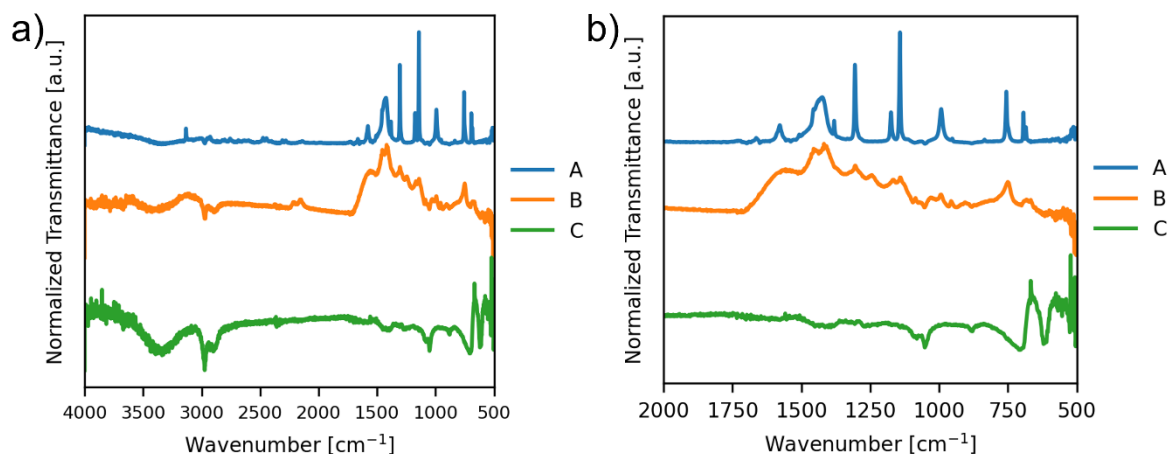


Fig. S21: FT-IR ATR data of pyrolyzed ZIF-67 a) the entire wavenumber region and b) a magnification of the fingerprint area. The capital letters in the legends refer to the points on the TGA curves in Fig. S20. A refers to the pristine ZIF-67, B is upon heating to 550 °C without any holding time, and C after the isothermal segment.

From the IR spectra, it is evident that the sample pyrolyzed at 550 °C without any holding time (marked as B) still contains the bonds characteristic of the pristine material (A). Even though the height of the peaks is smaller compared to the pristine material, all the characteristic bands are present. This clearly indicates that a complete decomposition of the organic linker has not taken place and hints that part of the pristine material is still present in the sample, but in a lower concentration. Differently, for the sample after prolonged pyrolysis at 550 °C for 12 h (C), the characteristic peaks of the linker are no longer observed, and we expect the MOF structure to have decomposed or restructured.

4. 1. 3 Comparison of the residual mass from TGA and *ex situ* measurements

Fig. S22 reports the comparison between the residual mass measured from TGA tests and the data obtained from *ex situ* measurements. While the extent of the mass loss measured for the sample treated in the tubular furnace is clearly lower with respect to the TGA, it is somehow compatible. Importantly the residual mass from TGA and the *ex situ* experiments tends to converge to similar values for long pyrolysis times. Here we ascribe the difference between the two sets of data to different thermal transfer properties of the TGA and the tube furnace (acting on the thermal convection and radiation) as well as the amount of sample used (thermal conduction).

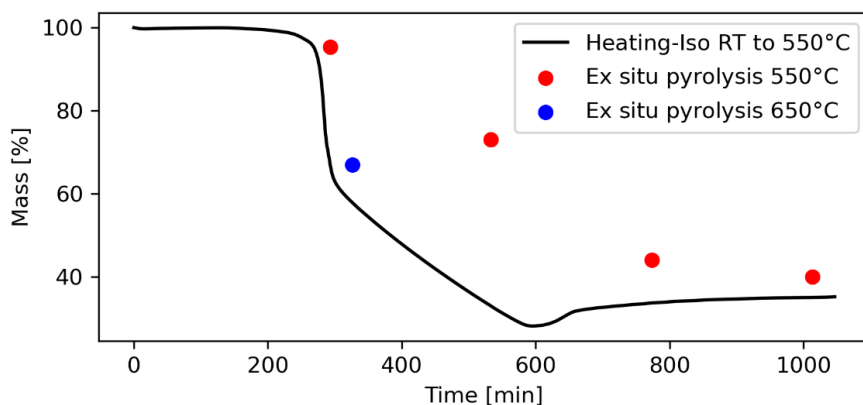


Fig. S22: Comparison between TGA data (black line) and *ex situ* experiments (filled symbols): The residual mass measured from the bulk *ex situ* pyrolysis experiment performed in a tubular furnace is shown as filled circles. Red and blue circles represent *ex situ* samples heated to 550 °C and to 650 °C, respectively. The *ex situ* data have been shifted on the x-axis to account for the time delay of the first isothermal step (at 70 °C, see temperature profiles in Fig. S20) present in the TGA measurements, but which was not applied in the preparation of the *ex situ* samples.

We expect the differences in the observed mass losses to be mostly due to heat transfer, due to difference in convective coefficients and conduction in the bulk of the material (given by the different amount of mass used in the two different experiments). Both the *in situ* and TGA experiments are tailored for obtaining an excellent heat transfer rate, and it is expected that the global heat transfer coefficient is markedly larger than for the tubular furnace. Thus, we do expect a significant delay in the *ex situ* experiment with 0 hours of holding time (as ZIF-67 is expected to have a low thermal conductivity). The differences between the *in situ* and *ex situ* techniques are supposed to be lower and lower with increasing holding time.

In summary, the data from TGA show that the system is most likely not in equilibrium, particularly for the fast heating (25 °C min^{-1}). This however is not necessarily the case for the *in situ* data, since we do not have any information regarding the heat transfer properties of such a system. We can however speculate that the *in situ* data could not be fully representative of the equilibrium (Fig. S19). After a threshold value of approx. 300 °C, the mass loss seems independent upon temperature, which is apparent from the comparison between the isotherms made at 550 °C and 800 °C. The data overlap and show that once the pyrolysis starts, the weight loss is independent on the temperature and only dependent on the pyrolysis time, i.e., the activation energy is extremely small (approaching zero).

4.2 Transmission electron microscopy (TEM)

Transmission electron microscopy (TEM) images were collected using a Talos FX-200 (Thermo Fischer Scientific). High angle annular dark field (HAADF) – scanning transmission electron microscopy (STEM) images were collected on the same microscope. STEM – energy dispersive X-ray (EDS) images were collected on the same Talos microscope with the ChemiSTEM system installed. Measurements were performed on the most heavily pyrolyzed samples, i.e., the 550 °C/ 12 h and the 650 °C/ 0 h to investigate their microstructural features and elemental contributions.

4.2.1 TEM investigations

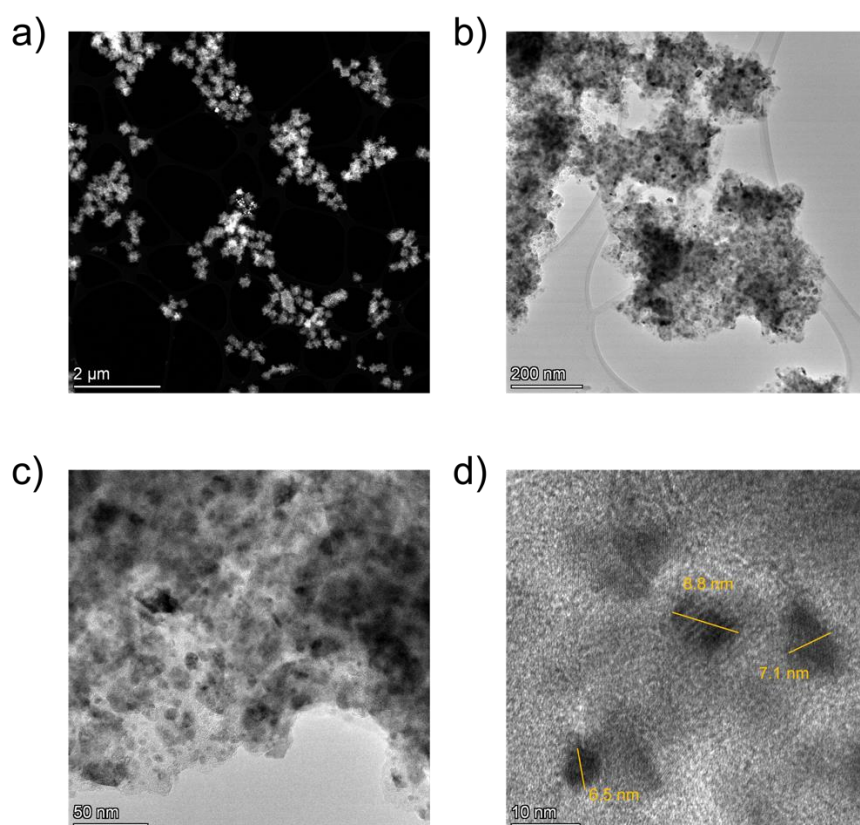


Fig. S23: TEM investigations on the 550 °C/ 12 h sample. a) HAADF image of the pyrolyzed MOF structures, indicating the preserved polyhedral morphology. b) TEM image indicating the original ZIF-67 particle size of approx. 200 nm. c) TEM image showing the particle structure with darker areas representing precipitation of small particles with a higher Z number embedded in a matrix. d) Magnification on a TEM image, allowing for an estimation of the embedded particle sizes (yellow bars represents the measured length of 6.5, 7.1 and 8.8 nm, respectively).

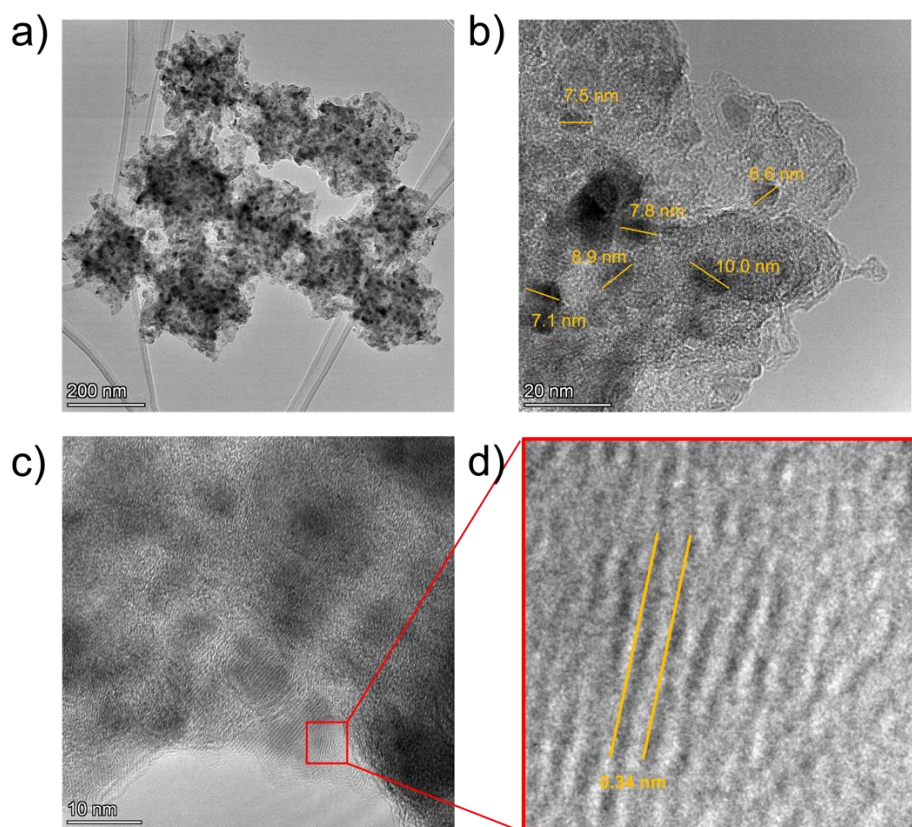


Fig. S24: TEM investigations on the 650 °C/ 0 h sample. a) The pyrolyzed MOF structures, indicating the preserved polyhedral morphology and an original ZIF-67 particle size of approx. 200 nm. b) TEM image showing the particle structure with darker areas representing small particles with a higher Z number embedded in a matrix. The embedded particle sizes are estimated (the yellow bars represent the measured lengths of 7.1, 7.8, 8.6, 8.9 and 10.0 nm, respectively). c) High resolution (HR) TEM indicating lattice fringes. d) Magnification on smaller area with the spacing between fringes in the marked area determined to 0.34 nm.

For both the 550 °C/ 12 h and the 650 °C/ 0 h samples the original polyhedral ZIF-67 morphology is preserved, with a particle size of approx. 200 nm (as also observed with SEM, manuscript Fig. 4). A precipitation of smaller dark particles with a higher Z number (attributed to Co, see STEM-EDS Fig. S25-26) is observed for both samples. These precipitated particles are embedded in a matrix. For the 550 °C/ 12 h sample, the average particle size is estimated to 7.5 ± 1.0 nm and for the 650 °C/ 0 h sample 8.0 ± 1.1 nm. Only the well-defined dark areas with particles in focus (with the yellow bars on Fig. S23d and Fig. S24b) are included in the average, and the error is taken as the standard deviation. These particle sizes fit well with what is determined from PDF refinements (see section 4.5) with a bimodal size distribution of 1.4 nm and 7.1 nm for the 550 °C/ 12 h sample and 1.7 nm and 9.4 nm for the 650 °C/ 0 h. We expect the nanoparticles with sizes of 1-2 nm would be visible with a higher TEM resolution and as also observed in other studies.⁷ The lattice fringes visible in Fig. S24d with a spacing of 0.34 Å corresponds well with the (100) lattice plane in Co fcc.

4.2.2 STEM-EDS

HAADF STEM-EDS performed on the most heavily pyrolyzed samples, *i.e.*, the 550 °C/ 12 h (Fig. S25) and the 650 °C/ 0 h (Fig. S26) indicate the formation of cobalt nanoparticles embedded in a nitrogen doped carbon matrix, as previously reported in literature.^{7,8} The selected areas include only Co particles and the nitrogen doped carbon matrix, and not the lacey carbon deposited on top of the Cu grid.

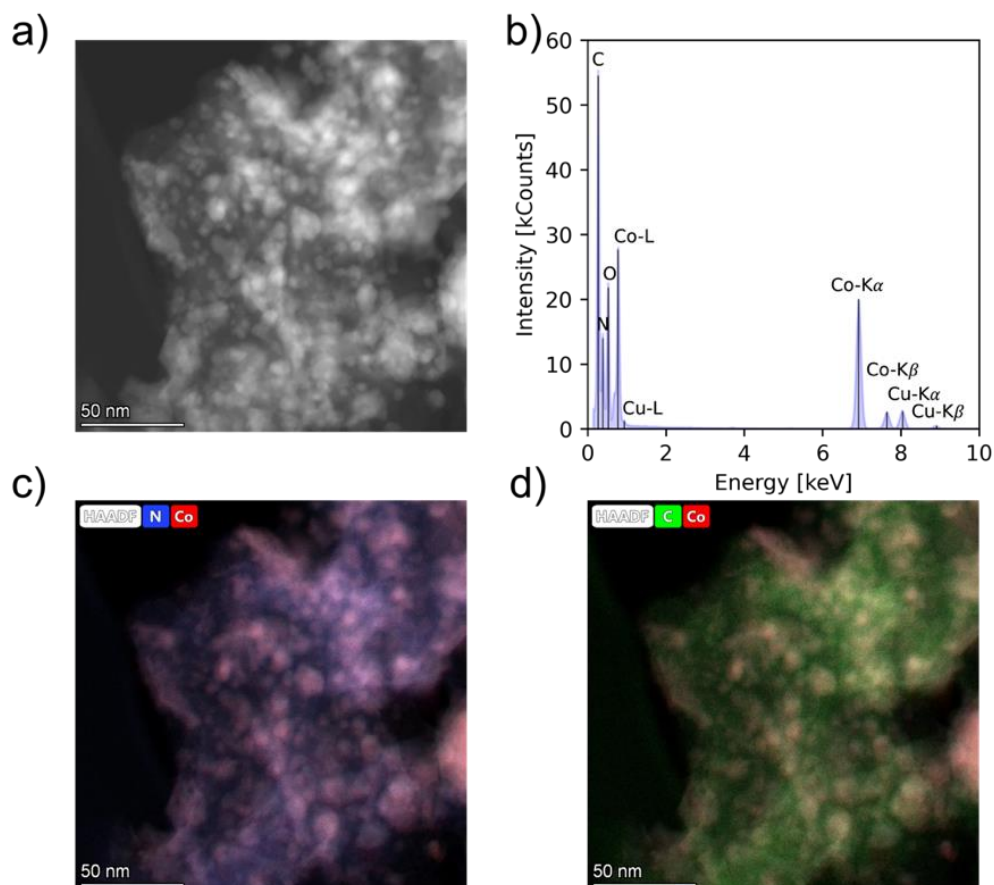


Fig. S25: Scanning transmission electron microscopy (STEM) performed on the 550 °C/ 12 h sample. a) High angle annular dark field (HAADF) image of the pyrolyzed ZIF-67. b) The summed spectrum with the major peaks indexed. Cu is due to the Cu grids used and the presence of oxygen is expected to be due to post oxidation upon exposure to air. c-d) EDS mapping of the ZIF-67 pyrolyzed at 550 °C/ 12 h with nitrogen and cobalt overlaid in c) and carbon and cobalt overlaid in d).

Table. S3: Results from the STEM-EDS measurement on one selected area on the 550 °C/ 12 h sample. No errors are associated with the fractions as only one area was measured. The fractions should be taken as representative rather than absolute values.

Z	Element	Atomic fraction	Mass fraction
6	C	62.3	40.5
7	N	11.4	8.63
8	O	14.5	12.5
27	Co	10.3	33.0
29	Cu	1.57	5.40

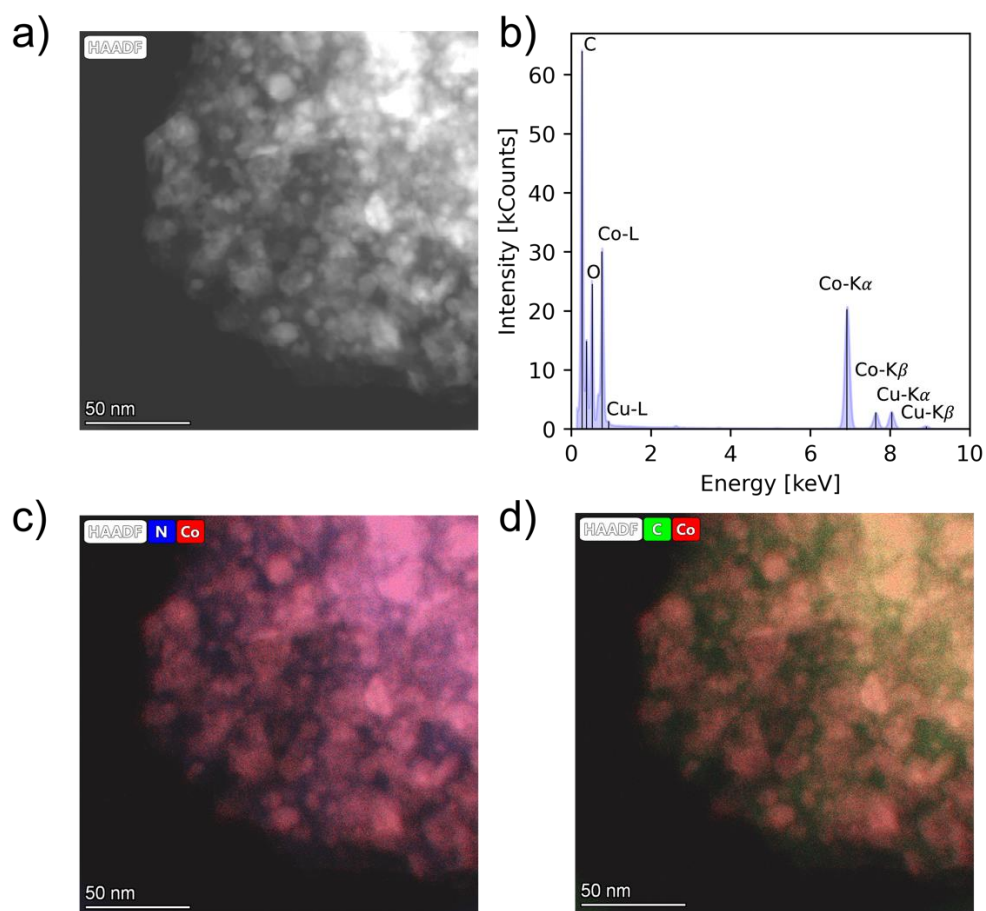


Fig. S26: STEM performed on the 650 °C/ 0 h sample. a) HAADF image of the pyrolyzed ZIF-67. b) The summed spectrum with the major peaks indexed. c-d) EDS mapping with nitrogen and cobalt overlaid in c) and carbon and cobalt overlaid in d).

Z	Element	Atomic fraction	Mass fraction
6	C	64.2	42.8
7	N	10.6	8.23
8	O	14.3	12.7
27	Co	9.54	31.2
29	Cu	1.45	5.10

Table. S4: Results from the STEM-EDS measurement on one selected area on the 650 °C/ 0 h sample. No errors are associated with the fractions as only one area was measured. The fractions should be taken as representative rather than absolute values.

4.3 Gas adsorption measurements

Nitrogen adsorption and desorption measurements were performed using a Quantachrome iQ2 Autosorb instrument at 77 K. Prior to measurements, samples were outgassed under inert gas flow for 16 hours at 100 °C. BET surface areas were estimated from data points in the P/P_0 range of 0.05-0.3.

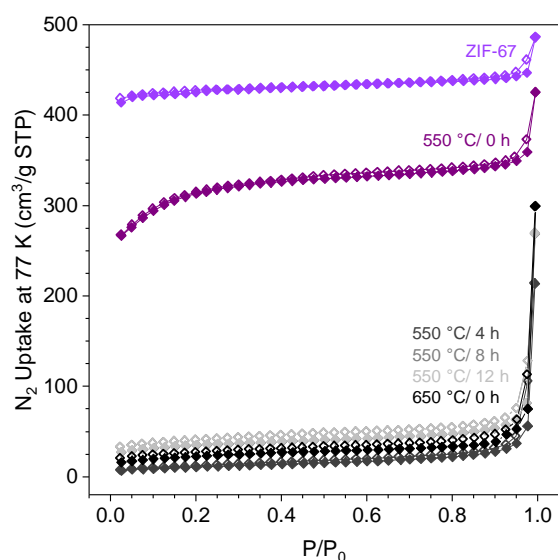


Fig. S27. Nitrogen adsorption/desorption isotherms for pristine and pyrolyzed ZIF-67 samples. Violet markers indicate data for the pristine sample, while data from pyrolyzed samples are indicated with dark purple (550 °C/ 0 h), dark grey (550 °C/ 4 h), dim grey (550 °C/ 8 h), light grey (550 °C/ 12 h) and black (650 °C/ 0 h). Adsorption data is indicated with closed markers, and desorption data is indicated with open markers.

Sample	BET surface area (m ² /g)
ZIF-67	1272
550 °C/ 0 h	905
550 °C/ 4 h	40
550 °C/ 8 h	42
550 °C/ 12 h	124
650 °C/ 0 h	79

Table S5: BET surface areas

As expected, the pristine ZIF-67 exhibits a BET surface area >1000 m²/g. As per TGA alone, the 650 °C/ 0 h sample would have intermediate characteristics between samples pyrolyzed at 550 °C for 0 and 4 hours, which is indeed the case, although significantly closer to the surface area of the 4 hour sample. The 550 °C/12 h sample stands out with the highest surface area of the samples pyrolyzed for longer time.

4.4 XAS

The Fourier transforms of the EXAFS data on the *ex situ* pyrolyzed samples were fitted with the scattering paths of either metallic cobalt (Fig. S28a) or ZIF-67 (Fig. S28b). Due to the information content of the data, it could not be justified doing multiphase fits. Thus, the EXAFS does not exclude the presence of residual ZIF-67 or cobalt oxide (for the 4 samples pyrolyzed at 550 °C for longer times or at 650 °C), however they indicate what the main phase is likely to be. The analysis was conducted with the Demeter package⁹

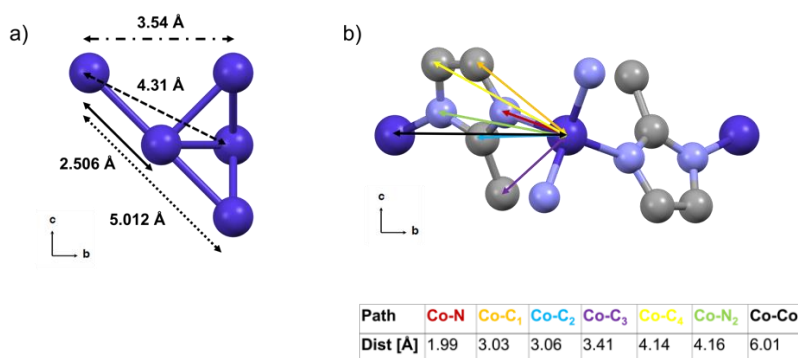


Fig. S28: a) Metallic cobalt and b) ZIF-67 scattering paths.

4.4.1 LCA fits

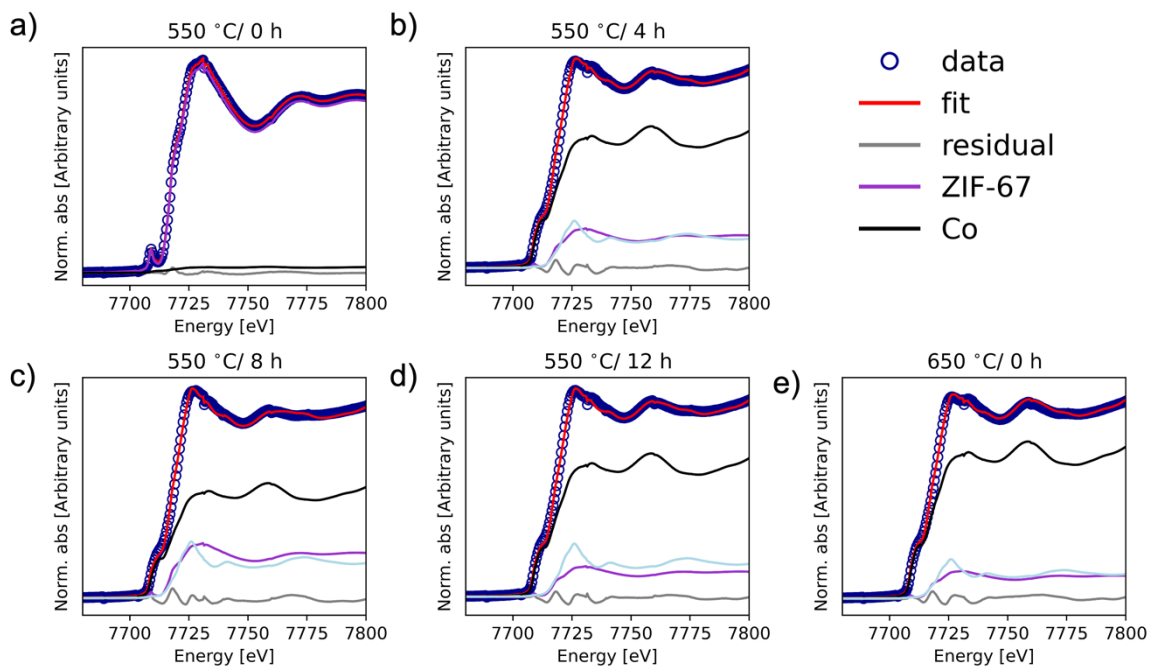


Fig. S29: LCA fitting against ZIF-67, a Co foil, and CoO. The sum of all weights was constrained to 1, and the weights were forced to be between 0 and 1. No E_0 shift was used.

Sample	550 °C/ 0 h	550 °C/ 4 h	550 °C/ 8 h	550 °C/ 12 h	650 °C/ 0 h
Weight ZIF-67	0.968(24)	0.164 (16)	0.235(17)	0.127(16)	0.115(88)
Weight Co	0.032(5)	0.680(11)	0.571(12)	0.695(11)	0.755(10)
Weight CoO	0(0)	0.156(77)	0.194(12)	0.178(11)	0.130(10)
R-factor	0.0002138	0.0012882	0.0016020	0.0014126	0.0011333
Chi-square	0.00508	0.02271	0.02998	0.02488	0.01917
Reduced Chi-square	0.0000564	0.0002551	0.0003368	0.0002796	0.0002154

Table S6: Fitted weight fractions along with the R-factors, Chi-square, and reduced chi-square. The weight fractions are given in cobalt percentages as retrieved from the analysis.

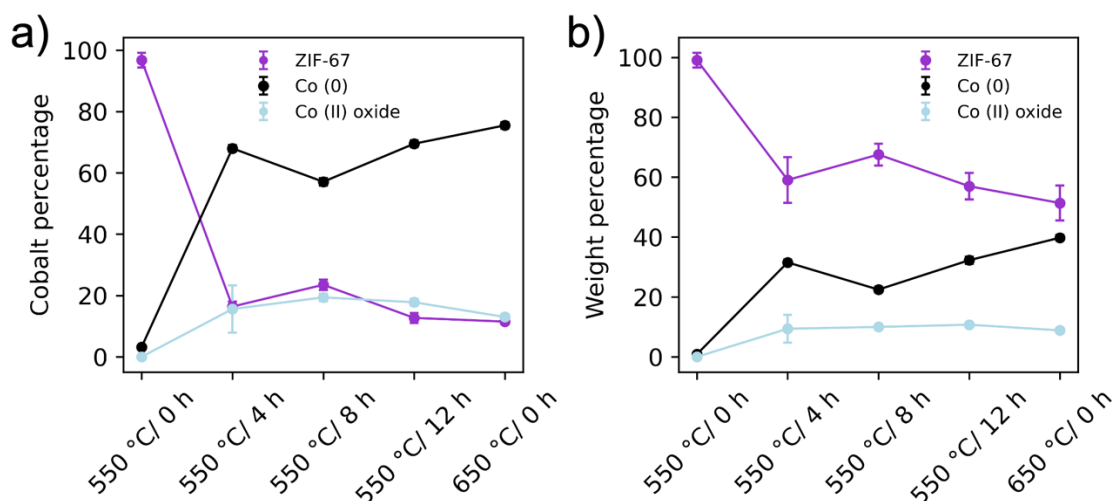


Fig. S30: Evolution of phases for LCA analysis with 3 reference samples. The weight of each reference is given as a) units of cobalt percentage and b) converted to a weight percentage.

At first glance there appears to be a discrepancy between the EXAFS (Fig. 5b) and the LCA analysis, as Co alone described the EXAFS of samples pyrolyzed at 4, 8, 12 hours and at 650 °C/ 0 h. We ascribe the difference to the fact that Co-Co scattering dominates the EXAFS over Co-N and Co-C correlations.

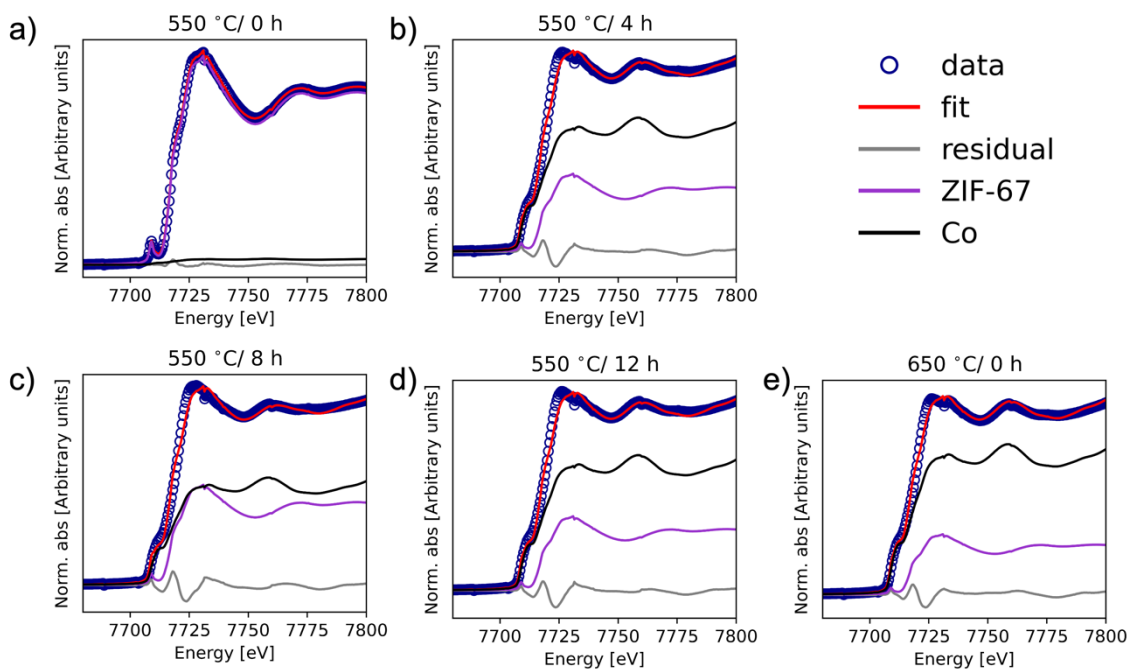


Fig. S31: LCA fitting against ZIF-67 and a Co foil, without including CoO as a component. The sum of all weights was constrained to 1, and the weights were forced to be between 0 and 1. No E_0 shift was used. Visibly worse fits are obtained with no CoO standards, as the white line is not properly described (compared with Fig. S29). The worse fit is also reflected in the Reduced Chi-square and the other goodness-of-fit parameters.

Sample	550 °C/ 0 h	550 °C/ 4 h	550 °C/ 8 h	550 °C/ 12 h	650 °C/ 0 h
Weight ZIF-67	0.968(24)	0.333(43)	0.445(24)	0.320(22)	0.256(29)
Weight Co	0.032(5)	0.667(20)	0.555(24)	0.680(25)	0.744(17)
R-factor	0.0002138	0.0044814	0.0062213	0.0055493	0.0034458
Chi-sqaure	0.00508	0.07900	0.1164	0.09774	0.05829
Reduced Chi-square	0.0000564	0.0008777	0.0012934	0.0010860	0.0006477

Table S7: Fitted weight fractions along with the R-factors, Chi-squared, and reduced chi-square. The weight fractions are given in cobalt percentages as retrieved from the analysis.

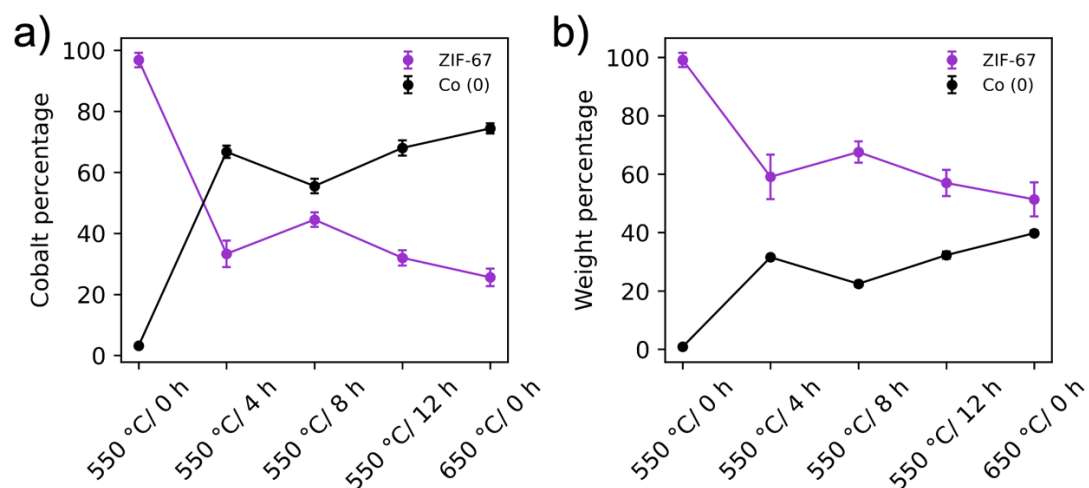


Fig. S32: Evolution of phases for LCA analysis with two components (ZIF-67 and Co). The weight of each standard is given in a) units of cobalt percentage and b) converted to a weight percentage.

4.5 PDF

4.5.1 The local to medium range order

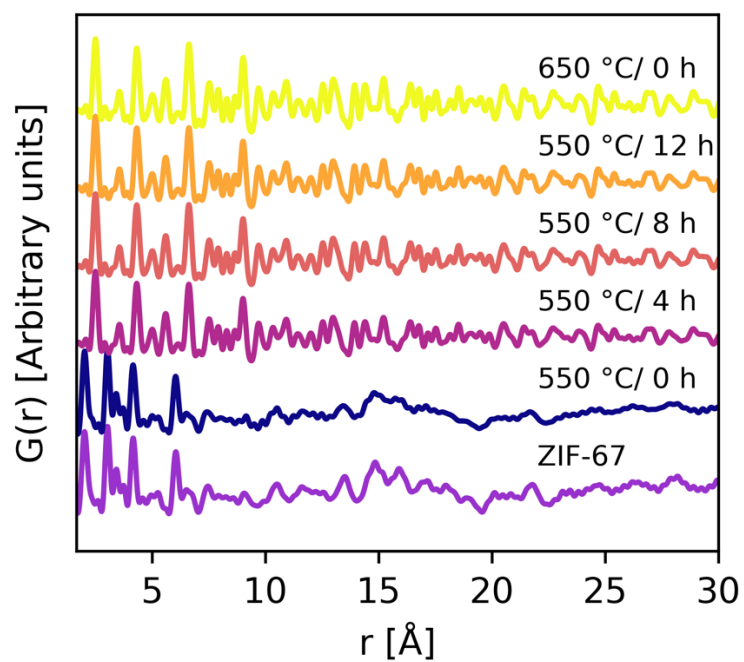


Fig. S33: The local to medium range order observed from PDFs of the *ex situ* pyrolyzed samples.

4.5.2 PDF fits

4.3.2.1 One phase refinements

The experimental parameters of Q_{damp} and Q_{broad} were fixed to the refined values of a LaB_6 standard, $2.960\text{e-}02 \text{ \AA}^{-1}$ and $2.094\text{e-}03 \text{ \AA}^{-1}$ respectively. All fits were performed with `diffpy.cmi`.¹⁰

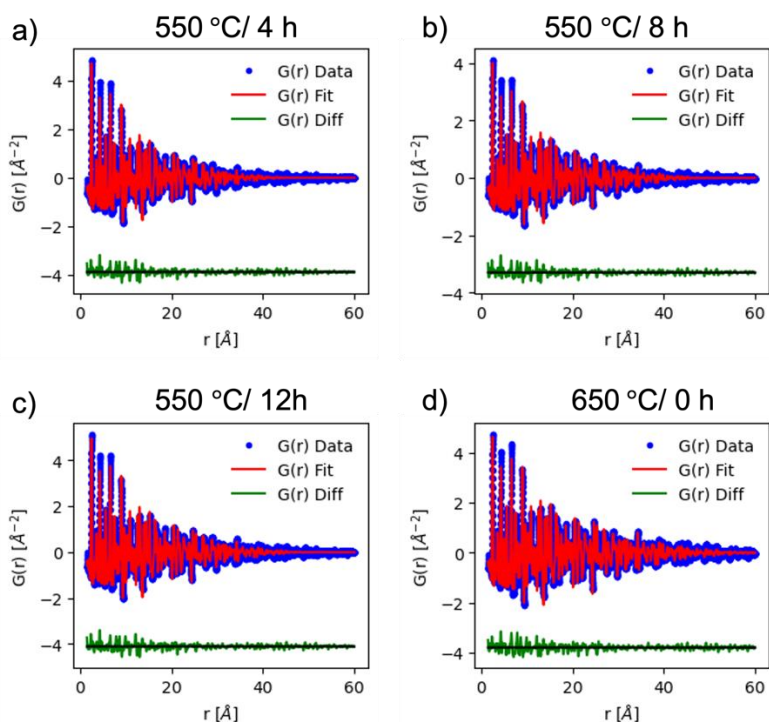


Fig. S34: “One phase” refinement of the PDF data on *ex situ* pyrolyzed samples for longer time durations. The data is fitted against the metallic Co fcc structure. The shape function does not correctly describe the data. The fits are underdetermined at low r , fits well in the middle, and is again worse at high r . This mismatch is seen in the residual ($G(r)$ Diff).

Sample	550 °C/ 4 h	550 °C/ 8 h	550 °C/ 12 h	650 °C/ 0 h
Scale	0.26(1)	0.22(1)	0.27(1)	0.25(1)
a [Å]	3.540(8)	3.541(8)	3.540(6)	3.542(5)
B_{iso} [Å ⁻²]	0.59(3)	0.57(3)	0.56(3)	0.52(2)
size [Å]	50(2)	55(2)	55(2)	72(3)
R_w	0.19	0.18	0.18	0.18

Table S8: One phase refinements against metallic Co fcc.

4.5.2.1 Two phase refinements

Sample	550 °C/ 4 h		550 °C/ 8 h		550 °C/ 12 h		650 °C/ 0 h	
Co Phase	1	2	1	2	1	2	1	2
Scale	0.18(2)	0.15(3)	0.17(2)	0.12(3)	0.20(2)	0.15(3)	0.19(2)	0.11(3)
a [Å]	3.54(0.9)	3.53(0.5)	3.54(0.9)	3.53(0.7)	3.54(0.7)	3.53(0.5)	3.54(0.5)	3.53(0.6)
B_{iso} [Å ⁻²]	0.56(6)	0.35(13)	0.55(5)	0.34(16)	0.53(4)	0.34(12)	0.50(3)	0.35(14)
size [Å]	65(6)	14(2)	70(7)	14(3)	71(6)	14(2)	94(10)	17(3)
R_w	0.143		0.145		0.141		0.155	

Table S9: Two phase refinements against metallic Co fcc with different size domains. To test the stability of the refinement, the initial guess values of the size parameters were varied from 10-100 Å for both phases in steps of 10. In 9 out of 10 refinements, the fits gave the same values. The R_w is improved from ~0.18 to ~0.14, consistently, compared to the one-phase refinements.

In addition to the one and two phase refinements against metallic Co, a two phase refinement with metallic Co and CoO and another with Co and CoN was also attempted. These are not included herein as they yielded unphysical values of the thermal displacement factors B_{iso} and unit cell parameter, a .

Other shape functions from *diffpy.srfit.pdf.characteristicfunctions* were also tested, *i.e.* spheroids and spherical nanoparticles with a lognormal distribution, although, compared to the two phase fit presented in the main article, these did not yield better results. Thus, we decided to interpret the data with the simplest model of spherical particles, as presented here.

Still, in an attempt to describe the underdetermined peaks at low r , and to investigate the order of the length scales, refinements with variable r -ranges were performed, just for the single phase.

4.5.2.3 Sliding boxcar refinements

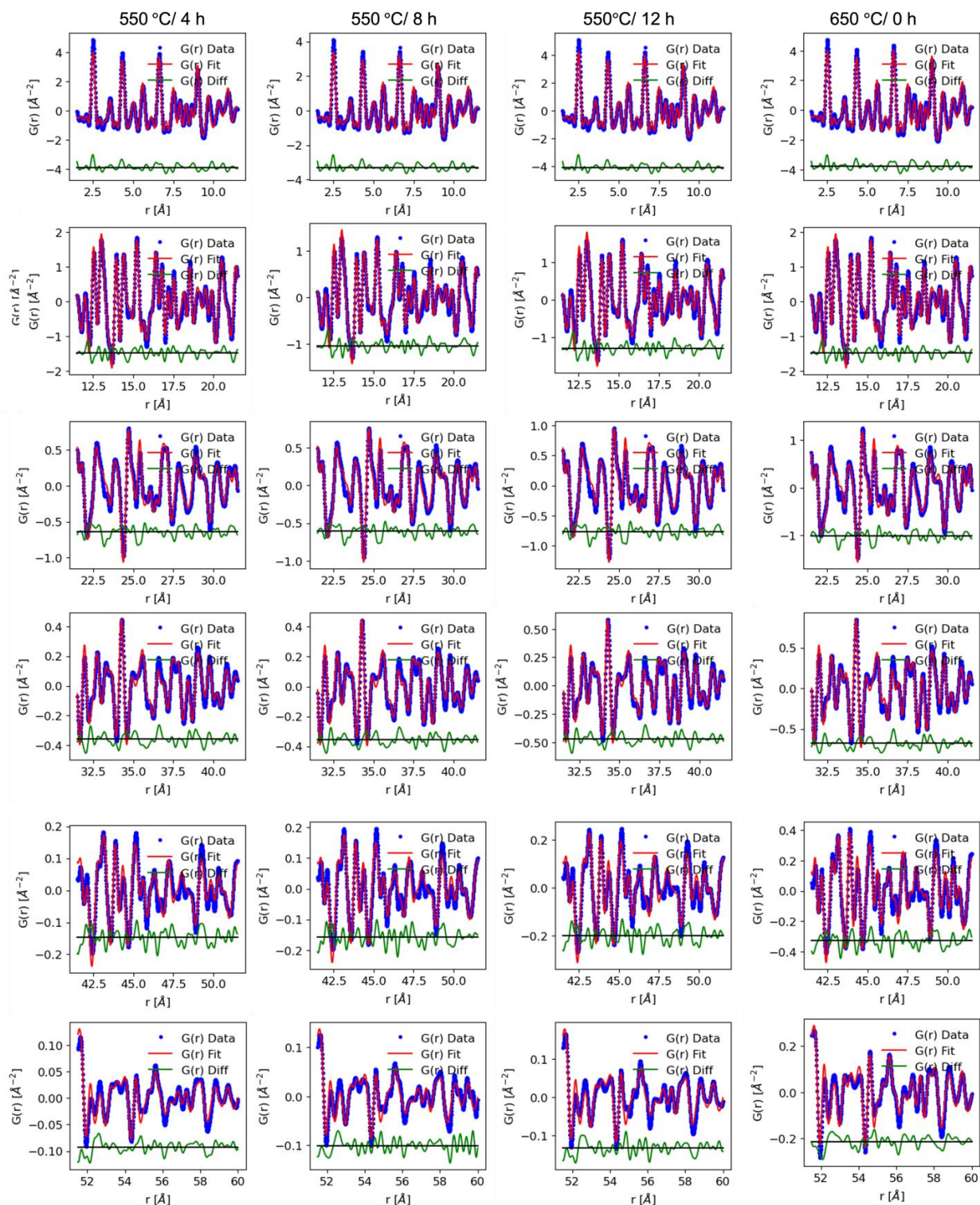


Fig. S35: One phase PDF fits with varying r -ranges. Both r_{\min} and r_{\max} are changed such that a window of 10 Å is fitted. The scale factors and the delta2 parameter are fixed to the refined values for the one-phase fit over the entire r -range to ensure sufficient information content in the fitted PDF region. Even for the first fits between 1.5 and 11.5 Å, the peaks of highest intensity are underdetermined.

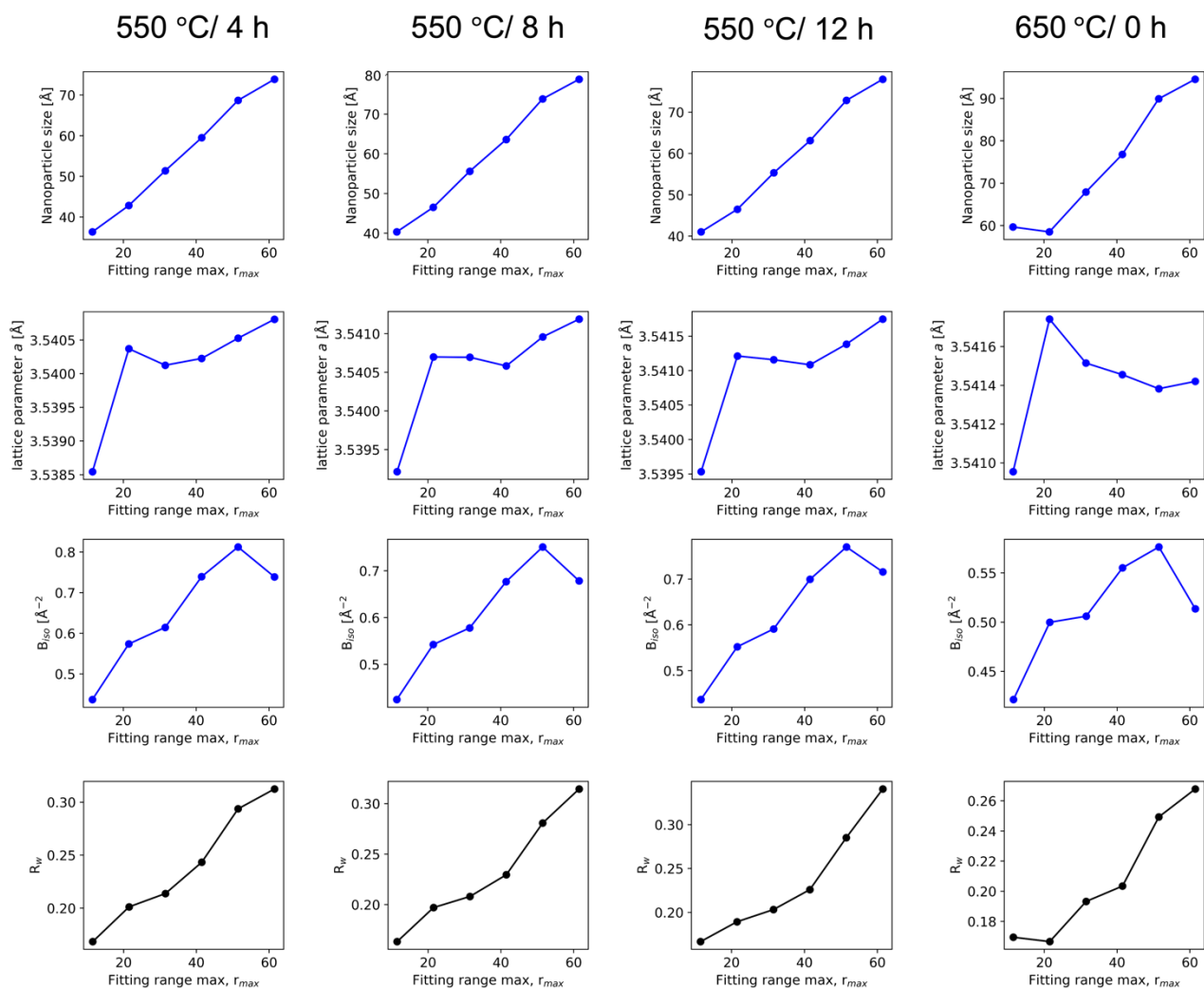


Fig. S36: Fitting results from the “one phase boxcar refinements” shown in Fig. S35. No value describing the average structure is approached. Instead, the parameters are seemingly steadily increasing. The almost linear increase in R_w values signify a worsening of the fittings.

4.5.2.3 Sliding r_{\max} refinements

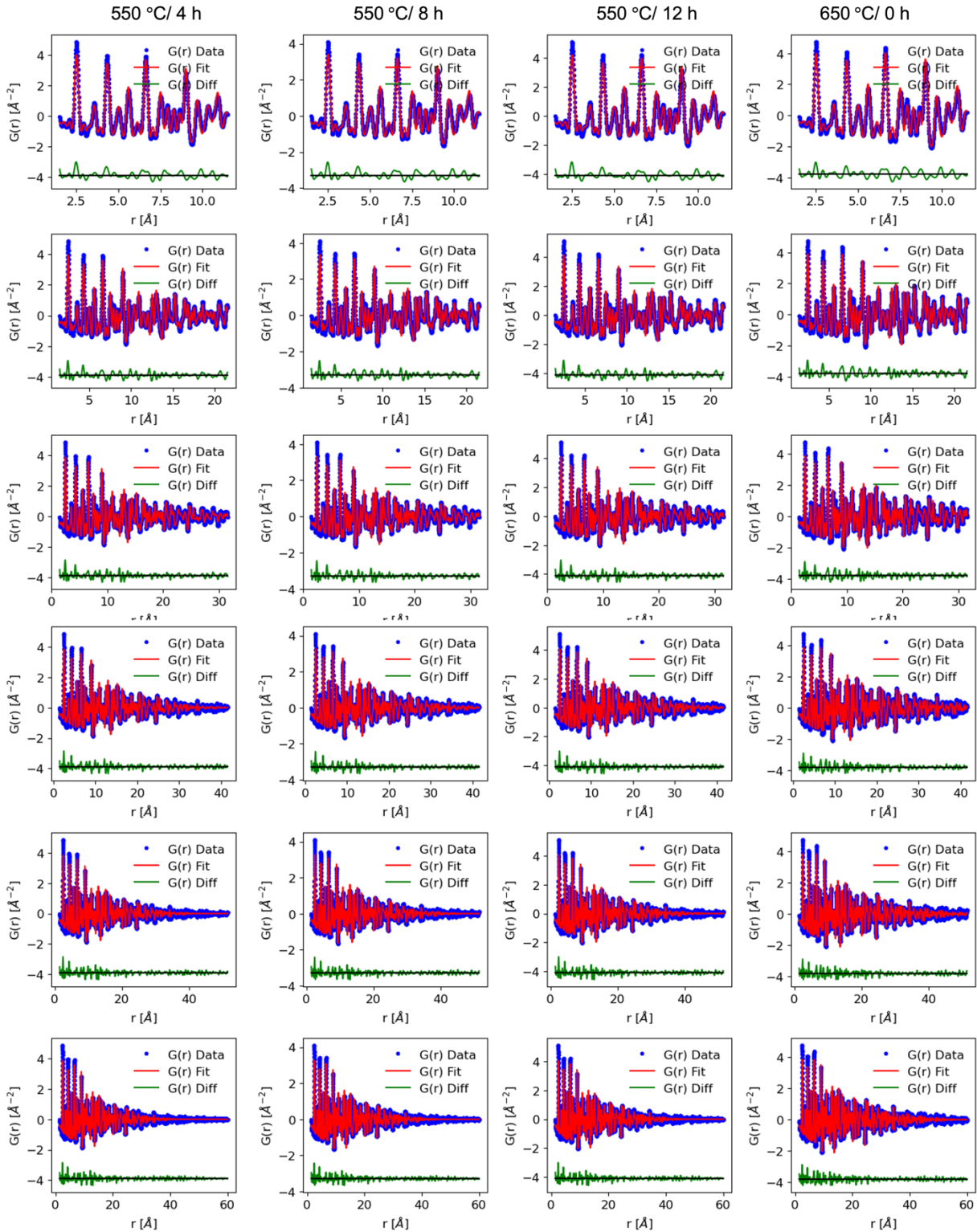


Fig. S37: One phase PDF fits with varying r -ranges. r_{\max} is increased in steps of 10 Å. The scale factors are set to the refined values for the one-phase fit over the entire r -range. The fits with an r_{\max} -value of 50 and 60 Å are significantly underdetermined at high r . All fits are underdetermined at low r .

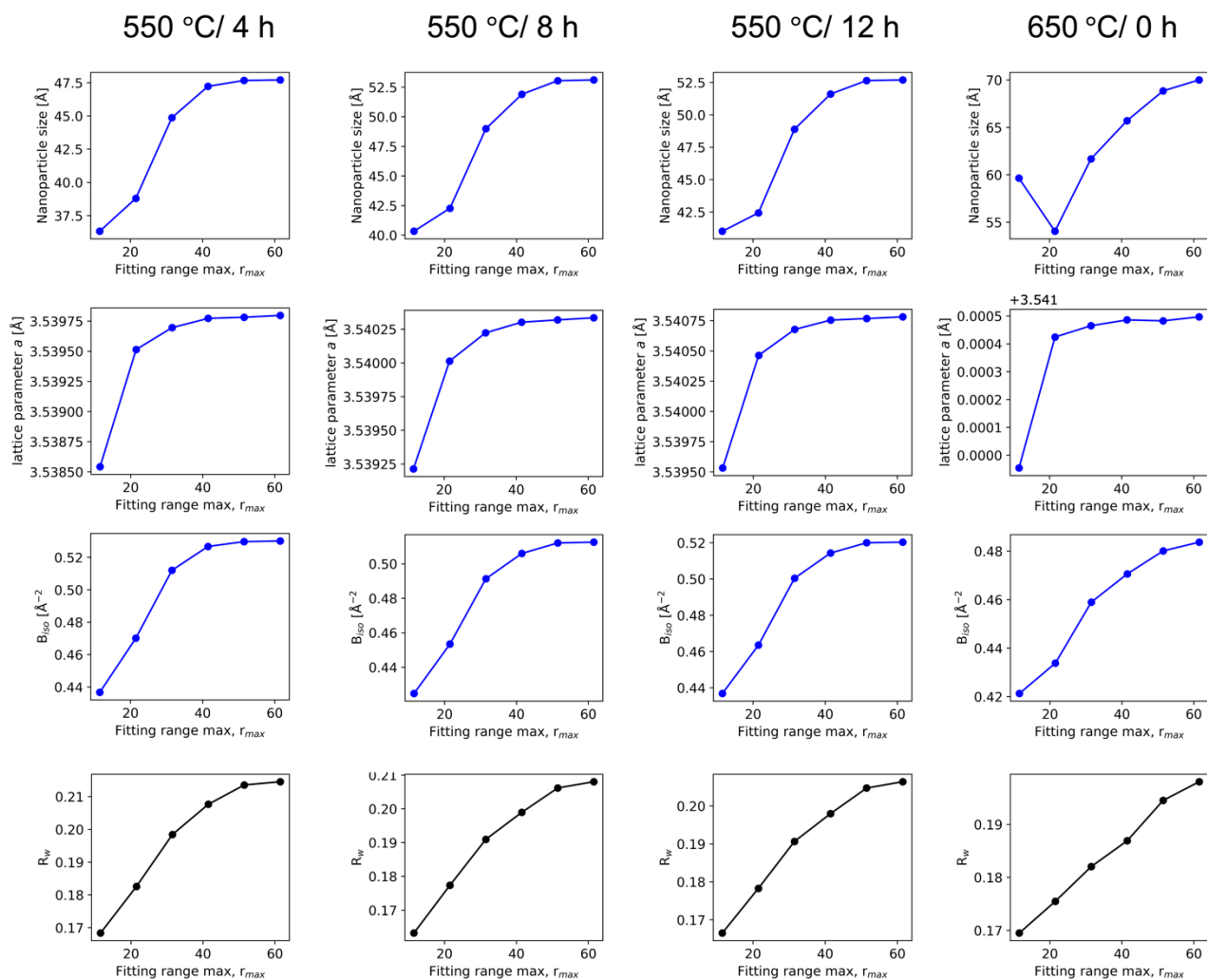


Fig. S38: Fitting results from the “one phase sliding r_{max} refinements” shown in Fig. S37. The nanoparticle size, the lattice parameter a , and the isotropic thermal displacement parameter B_{iso} all approach a steady value at higher r , whereas the R_w is increasing. It should be noted that the particle size that is approached is visibly too small as the data is not described at higher r .

4.5.3 NMF analysis

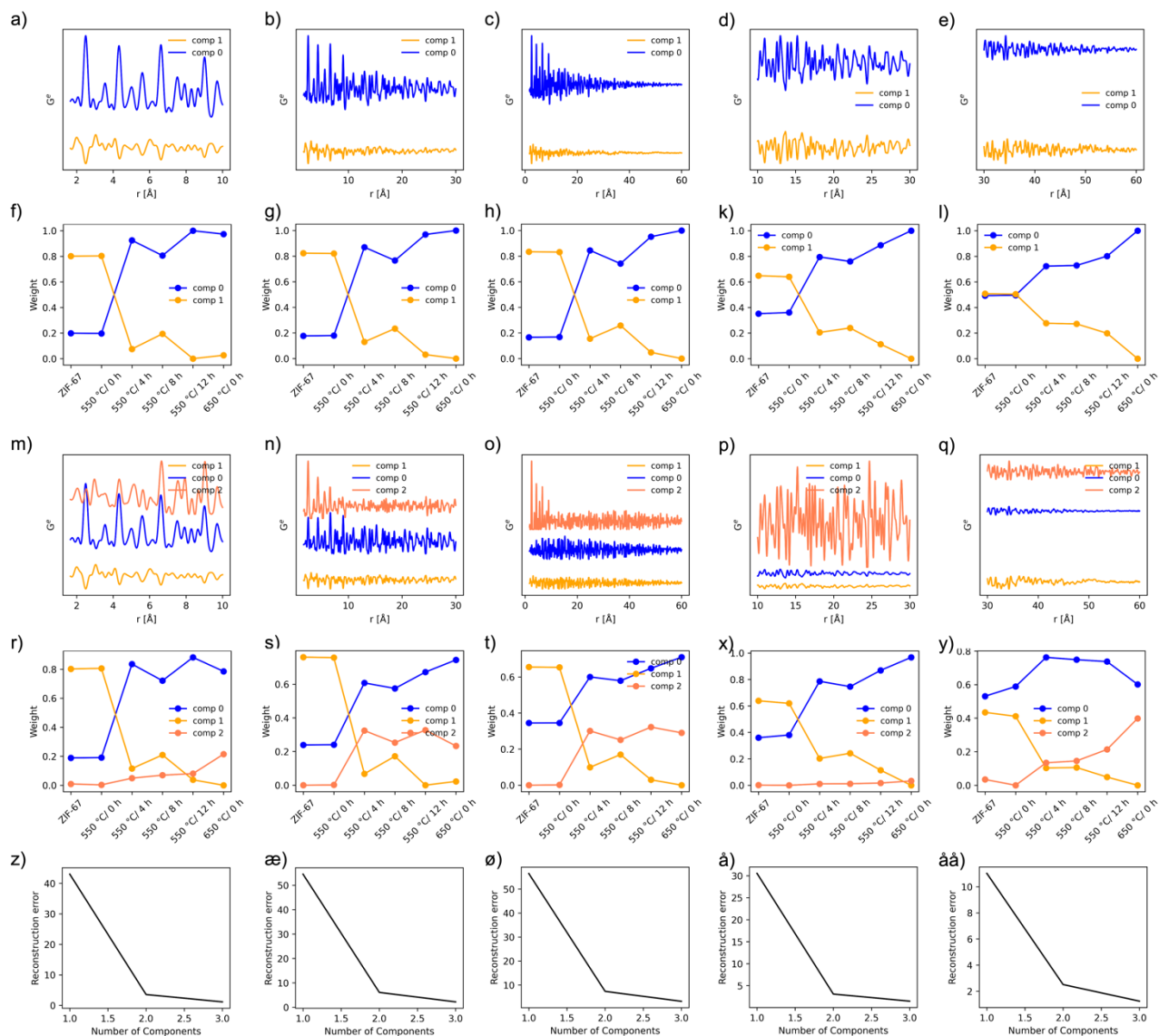


Fig. S39: a-e) NMF components for NMF analysis at different length-scales, with 2 components included. f-l) Evolution of the two components. m-q) NMF components for NMF analysis at different length-scales, with 3 components included. r-y) Evolution of the three components. z-aa) the reconstruction error for the two-component vs three-component analyses. In general, little improvement is observed upon including the third component.

5. Electrocatalytic OER

5.1 Linear sweep voltammetry (LSV)

Linear sweep voltammetry was performed with a scan rate of 10 mV s^{-1} recorded in $1 \text{ M KOH}_{(\text{aq})}$ electrolyte. For each catalyst, five consecutive sweeps were performed with stirring in between.

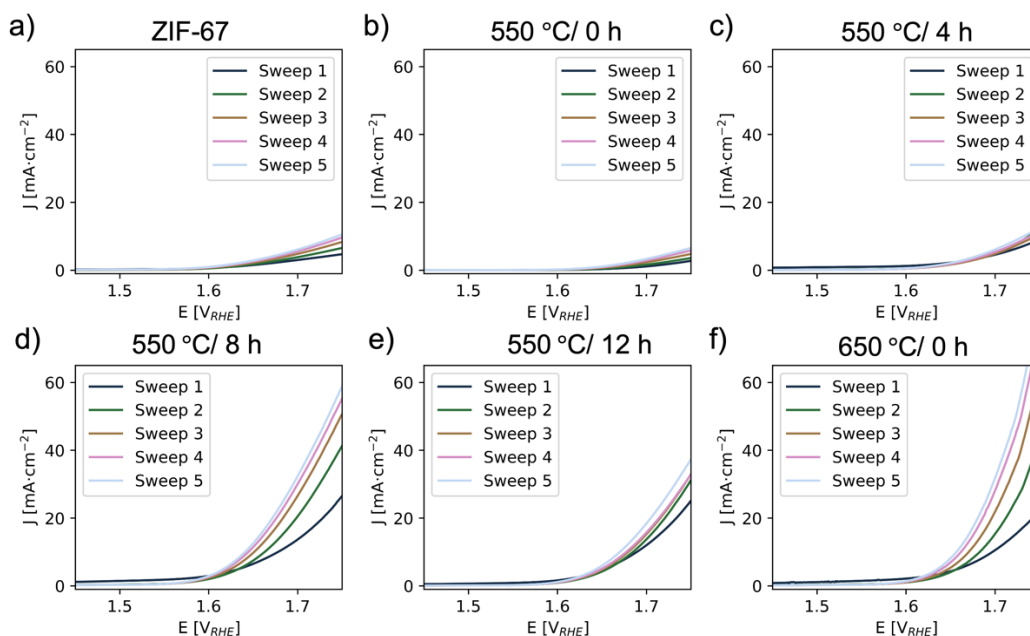


Fig. S40: Sweep 1-5 compared for each sample. The current density is calculated with a geometrical surface area of 1 cm^2 .

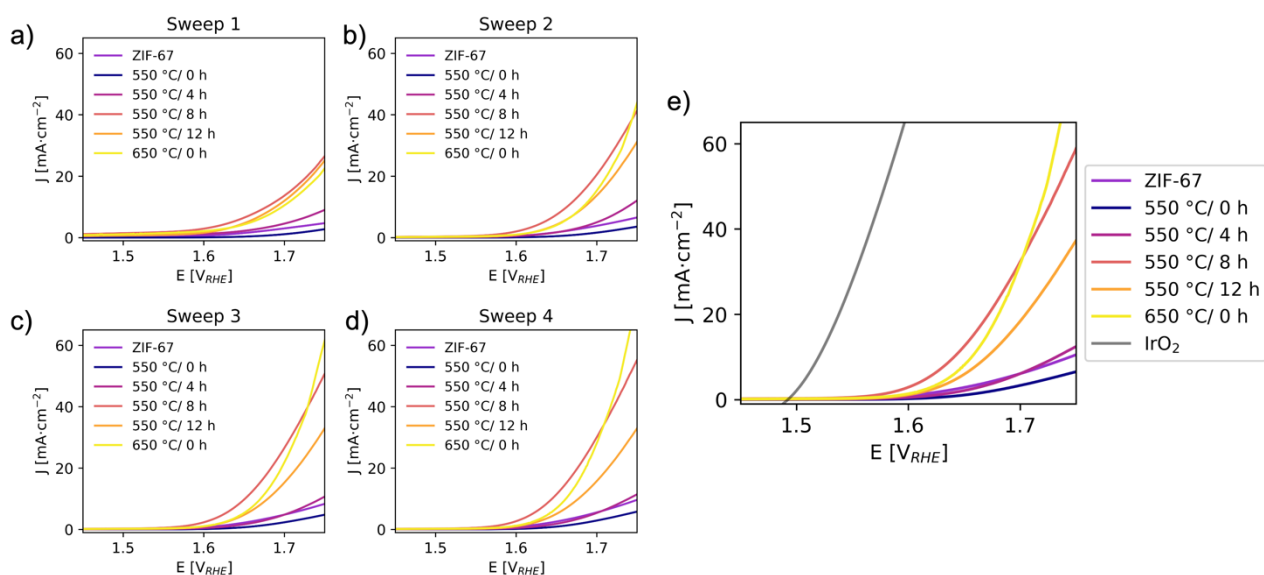


Fig. S41: Sweep 1 to 4 compared across the 6 different catalysts. e) Sweep 5 compared across the different catalysts and with the IrO_2 benchmark OER catalyst. The current density is calculated with a geometrical surface area of 1 cm^2 .

The overpotentials are estimated from the LSV curves, both as the intersection between a tangent to the steepest point on the slope, η_{slope} , and the baseline, and the potential at which the current density reaches 10 mA cm^{-2} , η_{current} (Fig. S38). Both methods show similar results.

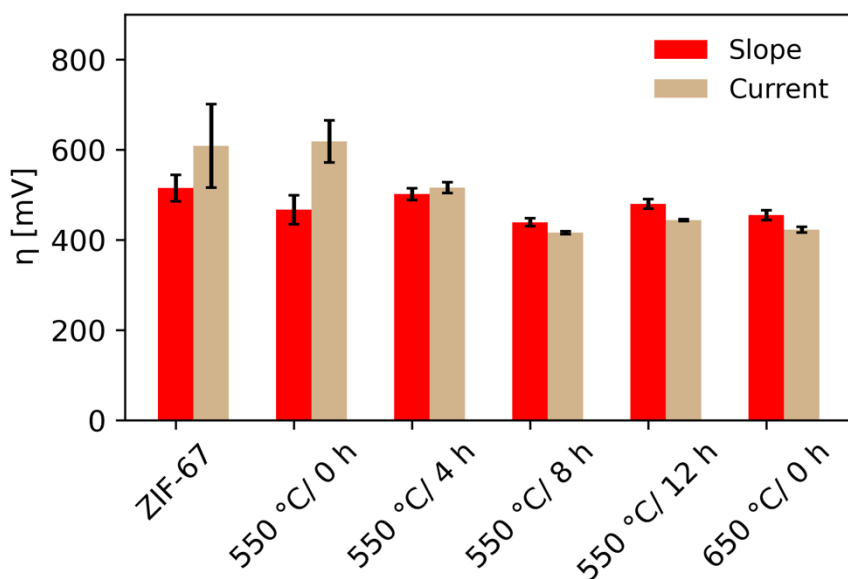


Fig. S42: The overpotentials η are determined for the linear sweep responses. For each catalyst the overpotential is determined from the intersection between a tangent to the steepest point on the slope and the baseline (red), along with the potential at which the current density reaches 10 mA cm^{-2} (nude).

5.2 Electrochemically active surface area (ECSA)

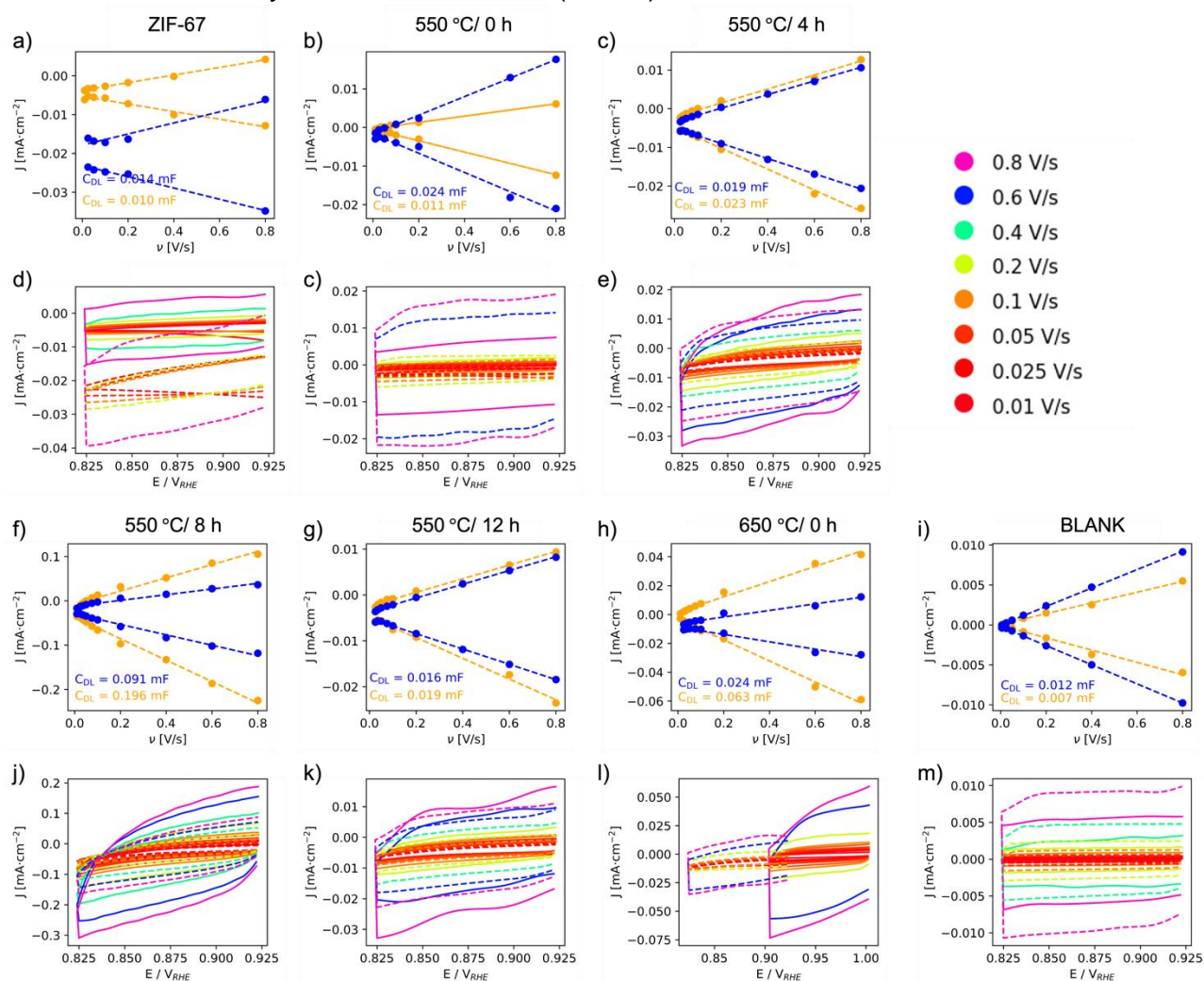


Fig. S43: Cyclic voltammetry recorded at different scan rates (as represented by the legend with colored filled symbols to the right-hand side of the figure) along with the current density calculated from a geometrical surface area of 1 cm^2 as a function of the scan rate. The dashed lines in the CV plots represent the sweeps before 2 hours of chronopotentiometry at $I = 10 \text{ mA}$, and the solid lines, after. A linear fit is obtained through regression, and the double layer capacitance C_{DL} is determined as the slope. The orange and blue lines represent the regression of before and after chronopotentiometry, respectively.

To determine the capacitance, cyclic voltammetry is recorded in a non-faradaic region, where we expect no peaks and the data to be correctly iR compensated (Fig. S43a-c and f-i). Both the positive and negative sweeps should be linear and have the same slope. It should be noted that for the pristine ZIF-67 the positive and negative slopes deviate from this as they are dissimilar. In addition, for the highest scan rates in Fig. S43e,k,m the sweeps are not completely linear. This is partially expected to be due to electrical noise in the potentiostat.

For the current versus scan rate plots, the data is expected to be linear and symmetrical with respect to the horizontal axis. For some of the experiments, an offset of the current is observed, this is especially evident for the pristine ZIF-67 after electrolysis.

5.3 Multistep electrolysis

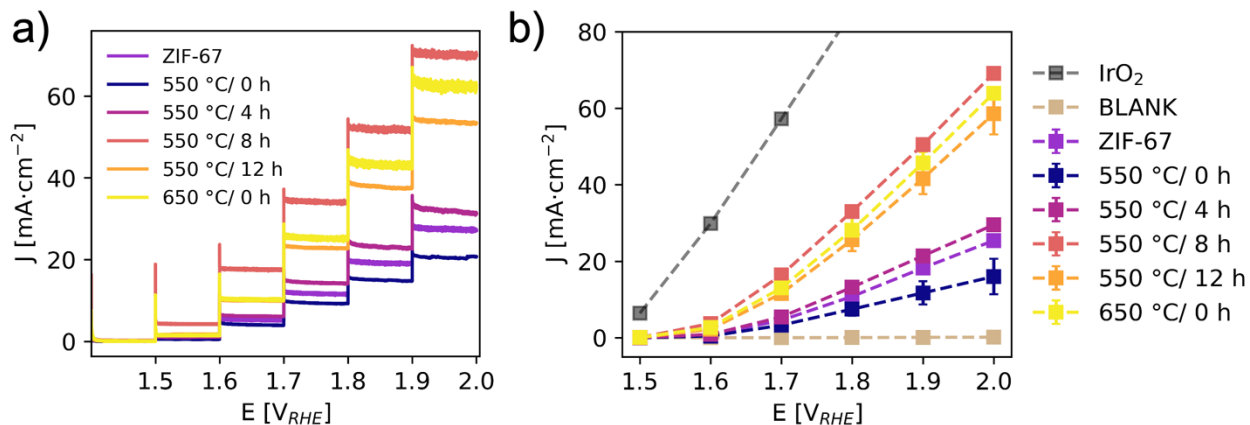


Fig. S44: Multistep electrolysis. a) Each potential is held for 20 s. b) The current density after stabilization. Data for the benchmarking catalyst of IrO₂ and BLANK carbon paper with no catalyst deposited are shown for comparison. The current density is normalized against the geometrical surface area.

5.4 Chronopotentiometry

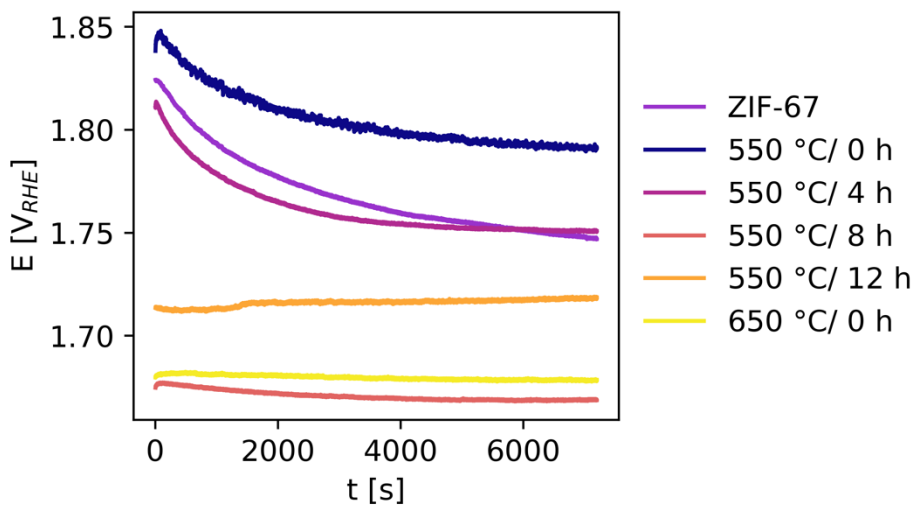


Fig. S45: Representative chronopotentiometry responses during 2 h measurements at $I = 10$ mA.

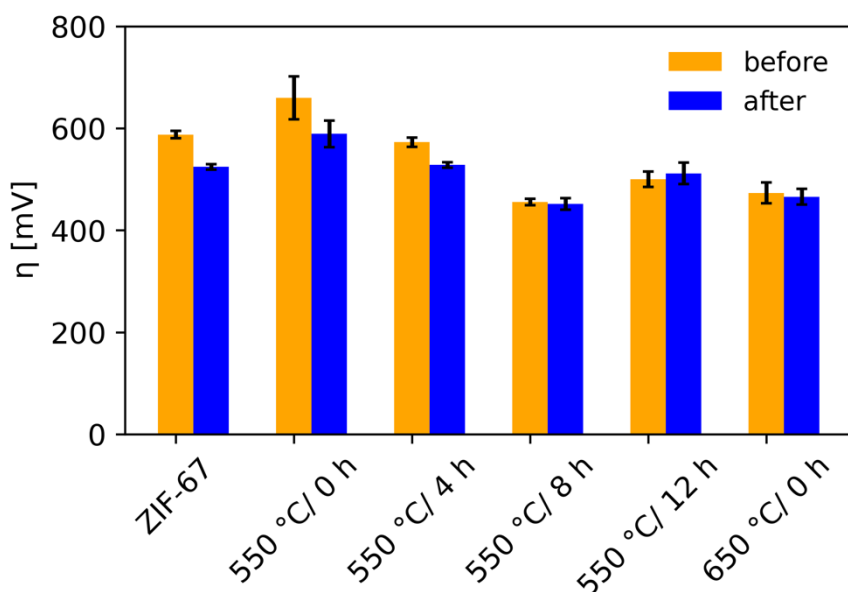


Fig. S46: Overpotentials determined from chronopotentiometry measurements at $I = 10$ mA, at the start of the experiment ($t = 0$) and after 2 h.

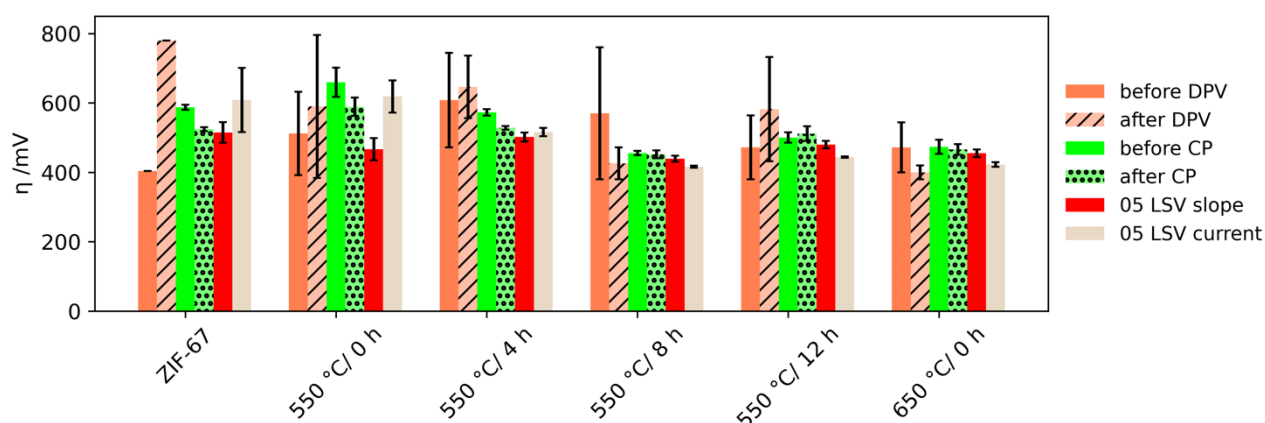


Fig. S47: Comparison of the different ways of determining the overpotentials. The overpotentials have been determined from differential pulse voltammetry (DPV), chronopotentiometry at $I = 10$ mA (CP) and linear sweep voltammetry both from linear regression (LSV slope) and at a current of 10 mA (LSV current). The DPV was measured both before and after 2 hours of chronopotentiometry, and the CP before and after refers to the overpotential at $t = 0$ and $t = 2$ h, respectively.

The overpotentials determined from DPV are less consistent with that from the other methods (Fig. S47). The other three methods give similar overpotentials, especially for the samples pyrolyzed at 550 °C for longer durations and at 650 °C/ 0 h.

5.5 Normalization to m_{Co} and ECSA

The mass of cobalt, m_{Co} , is calculated based on the mass after pyrolysis. It is assumed that the mass loss is entirely associated to the volatile organic linker.

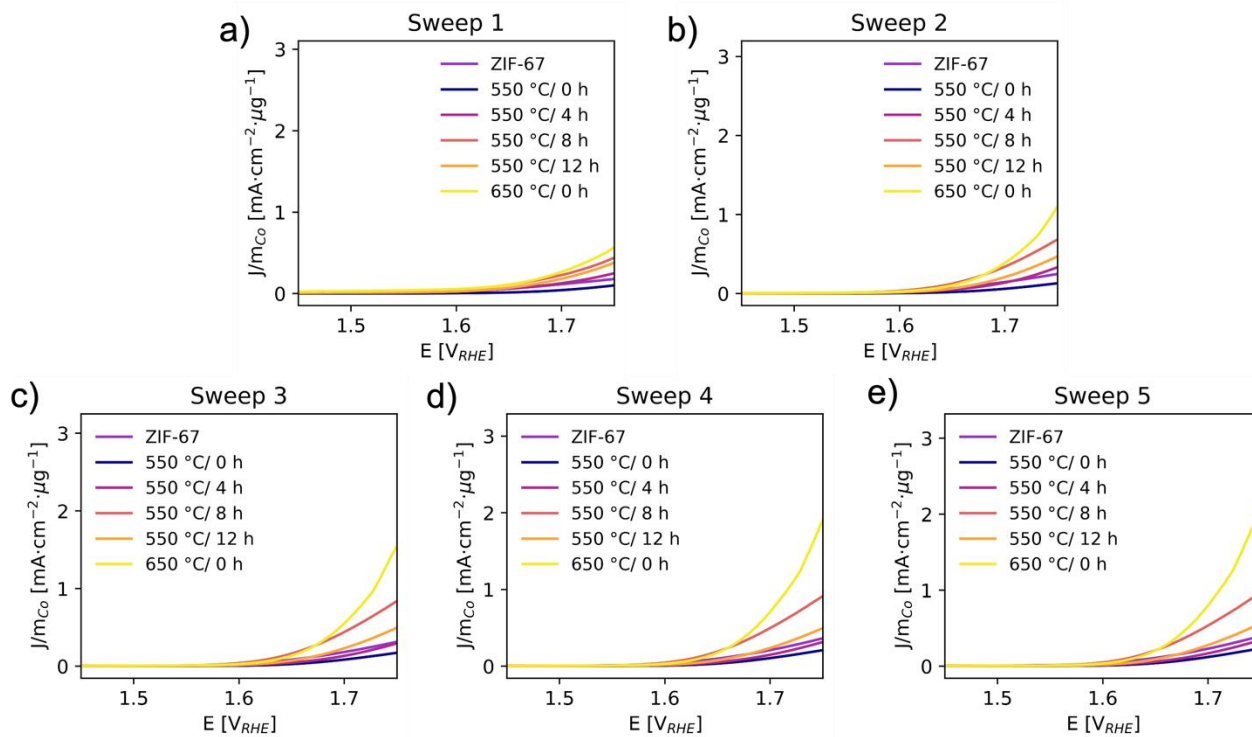


Fig. S48: LSV curves normalized to the mass of cobalt.

The mass of Co does not necessarily indicate the activity of Co, and for this reason we do not report calculations regarding the turn over frequency. While the current density normalized by the mass of Co is not used for TOF analysis, it is relevant from an engineering/economic perspective because it provides the actual amount of Co needed for the ink.

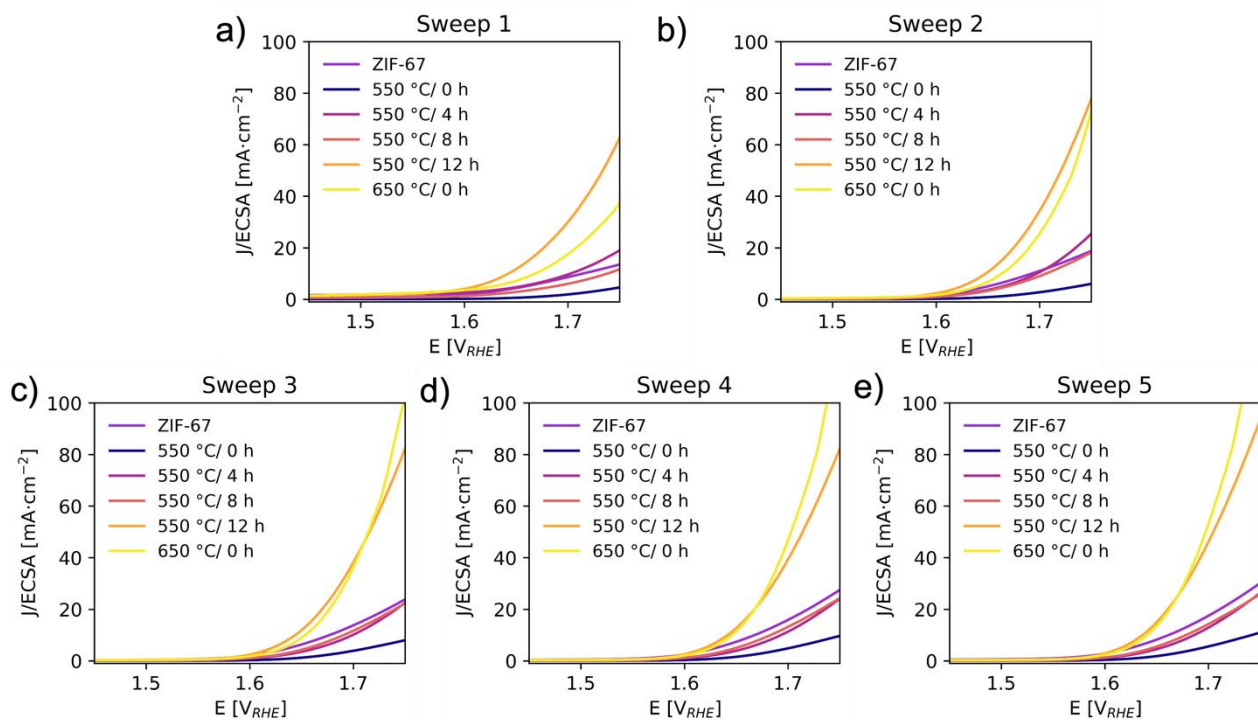


Fig. S49: LSV curves normalized to the ECSA determined from the initial set of capacitance measurements, *i.e.* right after the fifth sweep was recorded and before the 2 hours chronopotentiometry measurement.

5.6 Comparison with recent OER catalysts

The benchmarking of catalysts within the field of electrocatalysis in general is a huge challenge. Several factors influence performance and it can be hard to compare between literature when different setups and conditions have been used. With this in mind, we have attempted to compare the performance of different ZIF-67 derived catalysts, prepared through pyrolysis, as well as other Co-based catalysts, and the state-of-the-art IrO₂, as seen in Table S10. For a more extensive comparison with ZIF-67 derived catalysts, the reader is referred to the excellent review article by Jadhov *et al.*¹¹

Table S10: Reported OER catalysts prepared by pyrolyzing ZIF-67 with different approaches and the corresponding OER performance in alkaline media, as well as the performance of recent Co-based catalyst, and the state-of-the-art IrO₂.

Catalysts	Precursors	Annealing strategy	Electrolyte	Substrate	η_{10} [mV]	Reference
Pyrolyzed ZIF-67 based						
Pristine ZIF-67	ZIF-67	-	1 M KOH	Carbon paper	609	This work
Co NPs in N-C-matrix	ZIF-67	550 °C 8 h N ₂	1 M KOH	Carbon paper	416	This work
rGO-Co ₃ O ₄	ZIF-67 and graphene oxide	400 °C 2 h air	0.1 M KOH	Glassy carbon	450	Wu et al. ¹²
Co _x S _y -1000	ZIF-67 and H ₂ S	1000 °C 1 h H ₂ S	0.1 M KOH	Glassy carbon	470	Chen et al. ¹³
MSZIF-900	ZIF-67 on melamine sponge (MS)	900 °C 1 h N ₂	1 M KOH	3D porous MS	337	Jia et al. ¹⁴
Zn _{0.2} Co _{0.8} /NC	ZIF-67/ ZIF-8	800 °C 2 h N ₂	0.1 M KOH	Glassy carbon	292	Yang et al. ¹⁵
NC@Co-NGC DSNC	ZIF-67/ ZIF-8	800 °C 5 h N ₂ and H ₂ SO ₄ washing	O ₂ -saturated 0.1 M KOH	Glassy carbon rotating disk electrode	412	Liu et al. ¹⁶
Co ₉ S ₈ -NSC@Mo ₂ C	ZIF-67, 2-aminothiazole, benzoperoxidase, Mo ₂ C	800 °C (<i>no further information</i>)	1 M KOH	Glassy carbon	293	Luo et al. ¹⁷
CoNC-CNF-1000	ZIF-67/ ZIF-8, polyacrylonitrile-methylimidazole nanofibers	1000 °C 1 h N ₂	0.1 M KOH	Glassy carbon	452	Zhang et al. ¹⁸
CoCuNCN T@PC-700-2	ZIF-67 Cu-doped	700 °C 3 h Ar + 5% H ₂	1 M KOH	Carbon paper	340	Liu et al. ¹⁹
Co based						
Co/N-CNT	CoCl ₂ and cyanamide	700 °C 2 h Ar and H ₂ SO ₄ leaching	O ₂ -saturated 0.1 M KOH	Glassy carbon	392	Liu et al. ²⁰
Co/CeO ₂	CeO ₂ , CoCl ₂ and NaBH ₄	-	1 M KOH	Glassy carbon	365	Akbayrak et al. ²¹
Co ₃ O ₄	-	-	1 M KOH	Glassy carbon	455	Akbayrak et al. ²¹
State of the art						
IrO ₂	-	-	1 M NaOH	Glassy carbon	320	McCroary et al. ²²

Most of the reported preparation strategies for ZIF-67 derived catalysts involve multiple precursors, additional steps, and further modification. Our work focusses on the fundamental understanding of the pyrolysis step alone and explores the benefits of pyrolyzing at lower temperatures. The pyrolysis step is an integral part of the reported approaches, and thus we deem an understanding of the pyrolysis conditions, and the *in situ* mechanism, of paramount importance to decouple contributors to catalytic performance. In addition, in our work we are able to surpass the performance, in terms of lowering the overpotential, compared to multiple of the ZIF-67 derived catalysts prepared with further more advanced chemical/structural modifications. Of the ZIF-67 derived catalysts outperforming our work, a few of them perform significantly better than the noble-metal based state of the art IrO₂, which emphasizes the great potential of the ZIF-67 pyrolysis strategy.

References

1. R. Banerjee, A. Phan, B. Wang, C. Knobler, H. Furukawa, M. O'Keeffe and O. M. Yaghi, *Science*, 2008, **319**, 939-943.
2. Z. Thatcher, C. H. Liu, L. Yang, B. C. McBride, G. T. Tran, A. Wustrow, M. A. Karlsen, J. R. Neilson, D. B. Ravensbaek and S. J. L. Billinge, *Acta Crystallogr. A*, 2022, **78**, 242-248.
3. K. Momma and F. Izumi, *J. Appl. Crystallogr.*, 2011, **44**, 1272-1276.
4. C. L. Farrow, P. Juhas, J. W. Liu, D. Bryndin, E. S. Bozin, J. Bloch, T. Proffen and S. J. L. Billinge, *J. Phys.: Condens. Matter*, 2007, **19**.
5. A. Taylor and R. W. Floyd, *Acta Crystallogr.*, 1950, **3**, 285-289.
6. K. Suzuki, T. Kaneko, H. Yoshida, H. Morita and H. Fujimori, *J. Alloys Compd.*, 1995, **224**, 232-236.
7. Z. Wang, X. Ke, K. Zhou, X. Xu, Y. Jin, H. Wang and M. Sui, *J. Mater. Chem. A*, 2021, **9**, 18515-18525.
8. Y. Zhou, X. Deng, H. N. Xing, H. Y. Zhao, Y. B. Liu, L. S. Guo, J. Feng, W. Feng, Y. Zong, X. H. Zhu, X. H. Li, Y. Peng and X. L. Zheng, *Nano Res.*, 2022, **15**, 6819-6830.
9. B. Ravel and M. Newville, *J. Synchrotron Radiat.*, 2005, **12**, 537-541.
10. P. Juhas, C. L. Farrow, X. H. Yang, K. R. Knox and S. J. L. Billinge, *Acta Crystallogr. A*, 2015, **71**, 562-568.
11. H. S. Jadhav, H. A. Bandal, S. Ramakrishna and H. Kim, *Adv. Mater.*, 2022, **34**.
12. Z. L. Wu, L. P. Sun, M. Yang, L. H. Huo, H. Zhao and J. C. Grenier, *J. Mater. Chem. A*, 2016, **4**, 13534-13542.
13. B. L. Chen, R. Li, G. P. Ma, X. L. Gou, Y. Q. Zhu and Y. D. Xia, *Nanoscale*, 2015, **7**, 20674-20684.
14. G. Jia, W. Zhang, G. Z. Fan, Z. S. Li, D. G. Fu, W. C. Hao, C. W. Yuan and Z. G. Zou, *Angew. Chem. Int. Edit.*, 2017, **56**, 13781-13785.
15. X. B. Yang, J. Chen, W. S. Yang, H. Lin and X. T. Luo, *Inorg. Chem. Front.*, 2020, **7**, 4794-4794.
16. S. H. Liu, Z. Y. Wang, S. Zhou, F. J. Yu, M. Z. Yu, C. Y. Chiang, W. Z. Zhou, J. J. Zhao and J. S. Qiu, *Adv. Mater.*, 2017, **29**.
17. X. H. Luo, Q. L. Zhou, S. Du, J. Li, J. W. Zhong, X. L. Deng and Y. L. Liu, *ACS Appl. Mater. Interfaces*, 2018, **10**, 22291-22302.
18. W. M. Zhang, X. Y. Yao, S. N. Zhou, X. W. Li, L. Li, Z. Yu and L. Gu, *Small*, 2018, **14**.
19. G. Liu, B. Wang, P. Ding, W. Wei, Y. Ye, L. Wang, W. Zhu, H. Li and J. Xia, *J. Alloys Compd.*, 2020, **815**, 152470.
20. Y. Y. Liu, H. L. Jiang, Y. H. Zhu, X. L. Yang and C. Z. Li, *J. Mater. Chem. A*, 2016, **4**, 1694-1701.
21. M. Akbayrak and A. M. Önal, *Electrochim. Acta*, 2021, **393**.
22. C. C. L. McCrory, S. H. Jung, J. C. Peters and T. F. Jaramillo, *J. Am. Chem. Soc.*, 2013, **135**, 16977-16987.